25. Erdjument-Bromage, H. *et al.* Micro-tip reversed-phase liquid chromatographic extraction of peptide pools for mass spectrometry. *J. Chromatogr.* **826,** 157–181 (1998).
26. Geromanos, S., Freckleton, G. & Tempst, P. Tuning of an electrospray ionization source for maximum peptide-ion transmission into a mass spectrometer. *Anal. Chem.* **72,** 779–790 (2000).
27. Mann, M., Hojrup, P. & Roepstorff, P. Use of mass spectrometric molecular weight information to identify proteins in databases. *Biol. Mass Spectrom.* **22,** 338–345 (1993).
28. Mann, M. & Wilm, M. Error-tolerant identification of peptides in sequence databases by peptide sequence tags. *Anal. Chem.* **66,** 4390–4399 (1994).
29. Fenyö, D., Qin, J. & Chait, B. T. Protein identification using mass spectrometric information. *Electrophoresis* **19,** 998–1005 (1998).

Supplementary information is available at *Nature*'s World-Wide Web site (http://www.nature.com) or as a paper copy from the London editorial office of *Nature*.

Acknowledgements

We thank A. Nazarian and A. Grewal for help with mass spectrometric analysis, and the numerous people mentioned in 'Methods' for their gifts of antibodies. We also thank N. Francis, K.-M. Lee, S. Levine and A. Weiss for critical reading of the manuscript and E. Duprez and members of the Kingston lab for discussions and comments. A.J.S. is a Human Frontier Science Program Fellow. This work was supported by a NCI Cancer Center grant to P.T. and a NIH grant to R.E.K.

Correspondence and requests for materials should be addressed to R.E.K (e-mail: kingston@frodo.mgh.harvard.edu).

correction

Aβ peptide vaccination prevents memory loss in an animal model of Alzheimer's disease

Dave Morgan, David M. Diamond, Paul E. Gottschall, Kenneth E. Ugen, Chad Dickey, John Hardy, Karen Duff, Paul Jantzen, Giovanni DiCarlo, Donna Wilcock, Karen Connor, Jaime Hatcher, Caroline Hope, Marcia Gordon & Gary W. Arendash

Nature **408,** 982–985 (2000).

The caption to Fig. 1 should have included the following statement: "Two transgenic mice vaccinated with Aβ consistently failed to make choices in the radial arm water maze during the 15.5 month testing period and could not be included in the statistical analysis. Thus the sample size is smaller for the behavioural studies performed at 15.5 mo than at 11.5 mo."

All statistics, results (including means and standard errors in the figures), and the degrees of freedom and significance values in the text are correct as published. We have since replicated our findings with larger numbers of Aβ vaccinated transgenic mice ($n = 20$) whose performance in the radial arm water maze is again better than that of non-vaccinated transgenic mice. □

errata

LTRPC7 is a Mg·ATP-regulated divalent cation channel required for cell viability

Monica J. S. Nadler, Meredith C. Hermosura, Kazunori Inabe, Anne-Laure Perraud, Qiqin Zhu, Alexander J. Stokes, Tomohiro Kurosaki, Jean-Pierre Kinet, Reinhold Penner, Andrew M. Scharenberg & Andrea Fleig

Nature **411,** 590–595 (2001).

In this Letter, the following sentence should have appeared in the Acknowledgements section: "We gratefully acknowledge technical advice, the MerCreMer plasmid[1], and the MerCreMer transfected DT-40 cell line necessary for the creation of the Cre-Lox inducible LTRPC7 knockout cell lines from M. Reth and T. Brummer". □

1. Zhang, Y., Wienands, J., Zurn, C. & Reth, M. Induction of the antigen receptor expression on B lymphocytes results in rapid competence for signaling of SLP-65 and Syk. *EMBO J.* **17,** 7304–7310 (1998).

Coexistence of superconductivity and ferromagnetism in the *d*-band metal $ZrZn_2$

C. Pfleiderer, M. Uhlarz, S. M. Hayden, R. Vollmer, H. v. Löhneysen, N. R. Bernhoeft & G. G. Lonzarich

Nature **412,** 58–61 (2001).

In Fig. 2 the temperature axis has erroneously been multiplied by a factor of ten. These values should read 0.1 K to 0.6 K. □

Supplementary Information for more details) in serum samples (200 μl of blood) collected at 13 and 25 weeks.

Behavioural tests and data analysis

The water maze apparatus, mouse handling and general testing procedures have been described[23]. Before the first spatial learning test at 11 weeks, all mice underwent non-spatial pre-training (NSP) to assess swimming abilities and to accustom mice to the test[24,25] (see Supplementary Information). Two days after the NSP phase, all mice underwent a reference memory training with a hidden platform placed in the centre of one quadrant of the pool for 5 days, with four trials per day. After the last trial of day 5, the platform was removed from the pool and each mouse received one 60-s swim probe trial. Escape latency (s), length of swim path (cm), swim speed (cm s^{-1}), % of floating (speed less then 5 cm s^{-1}), % of time in outer zone (near the pool wall), and % of time and path in each quadrant of the pool were recorded using an on-line HVS image video tracking system[23] (see Supplementary Information).

For the probe trials, an annulus-crossing index was calculated that represents the number of passes over the platform site, minus the mean of passes over alternative sites in other quadrants. The index expresses the spatial place preference and controls for alternative search strategies without place preferences, such as circular search paths[26,27]. All mice were re-tested at 15, 19 and 23 weeks of age, one week before the next immunization. At each re-testing, the platform was placed in the centre of a different, semi-randomly chosen pool quadrant for all five sessions of training. At the end of the experiment, all mice were given a cue (visual platform) learning test. This was followed by the open-field test to investigate spontaneous locomotor exploration. Behavioural data was analysed using a mixed model of factorial ANOVA. Degrees of freedom were adjusted by Greenhouse–Geisser epsilon correction for heterogeneity of variance. A Bonferroni Inequality correction was applied for multiple comparisons. Omega squared (ω^2) was used as a measure of effect size caused by different factors.

Analysis of βAPP and amyloid burden in brain

Three 5-μm sections at 25-μm intervals from one cerebral hemisphere were immunostained with Dako 6F/3D anti-Aβ monoclonal antibody to residues 8–17 (which is primarily reactive against dense-cored plaques) with 4G8 (ref. 28), or with sera from immunized mice, and counterstained with haematoxylin and resin mounted as described (M.A.C. *et al.*, manuscript in preparation). For some samples the formic-acid treatment step was omitted. End products were visualized with diaminobenzidine. Amyloid plaque burden was assessed using Leco IA-3001 image analysis software interfaced with a Leica microscope and a Hitachi KP-M1U CCD video camera. The quantitative analysis was performed at of × 25 magnification, and the image frame and guard size was set to 0,0,639,479 (307,200 μm^2) for each slide. The brain area (cortex or hippocampus) was outlined using the edit plane function, and the area and number of plaques in the outlined structure were recorded. Data were pooled for all three sections.

Cerebral Aβ levels were assayed from formic-acid-extracted[29], hemi-brain sucrose homogenates using an ELISA method (see Supplementary Information) in which Aβ was trapped with either monoclonal antibody to $Aβ_{40}$ (JRF/cAb40/10) or $Aβ_{42}$ (JRF/cAb42/26) and then detected with horseradish peroxidase (HRP)-conjugated JRF/Abtot/17. The dilution of JRF/Abtot/17 and samples were optimized to detect Aβ in the range of 50 to 800 fmol ml^{-1}. ELISA signals are reported as the mean ± s.e.m. of four replica wells in fmol Aβ per mg total protein (determined with the BioRad DC protein assay), based on standard curves using synthetic $Aβ_{1–40}$ and $Aβ_{1–42}$ peptide standards (American Peptide Co. Sunnyvale, CA). Cerebral βAPPs levels were analysed in supernatant of brain as described[30].

Received 19 July; accepted 16 November 2000.

1. Steiner, H., Capell, A., Leimer, U. & Haass, C. Genes and mechanisms involved in beta-amyloid generation and Alzheimer's disease. *Eur. Arch. Psychiat. Clin. Neurosci.* **249,** 266–270 (1999).
2. Schenk, D. *et al.* Immunization with Aβ attenuates Alzheimer's disease-like pathology in the PDAPP mouse. *Nature* **400,** 173–177 (1999).
3. Bard, F. *et al.* Peripherally administered antibodies against amyloid beta-peptide enter the central nervous system and reduce pathology in a mouse model of Alzheimer disease. *Nature Med.* **6,** 916–919 (2000).
4. Whitehouse, P. J. *et al.* Clinical trial designs for demonstrating disease-course-altering effects in dementia. *Alzheimer Dis. Assoc. Disord.* **12,** 281–294 (1998).
5. Morris, R. Developments of a water-maze procedure for studying spatial learning in the rat. *J. Neurosci. Methods* **11,** 47–60 (1984).
6. Markowska, A. L., Long, J. M., Johnson, C. T. & Olton, D. S. Variable-interval probe test as a tool for repeated measurements of spatial memory in the water maze. *Behav. Neurosci.* **107,** 627–632 (1993).
7. Martin, P. & Bateson, P. *Measuring Behaviour* (Cambridge Univ. Press, Cambridge, 1996).
8. Hsiao, K. Correlative memory deficits, Aβ elevation, and amyloid plaques in transgenic mice. *Science* **274,** 99–102 (1996).
9. Rogers, S. L., Farlow, M. R., Doody, R. S., Mohs, R. & Friedhoff, L. T. A 24-week, double-blind, placebo-controlled trial of donepezil in patients with Alzheimer's disease. Donepezil study group. *Neurology* **50,** 136–145 (1998).
10. Terry, R. D., Masliah, E. & Hansen, L. A. in *Alzheimer Disease* 2nd edn (eds Terry, R. D., Katzman, R., Bick, K. C. & Sisodia, S. S.) (Lippincott Williams Wilkins, Philadelphia, 1999).
11. Moechars, D. *et al.* Early phenotypic changes in transgenic mice that over-express different mutants of amyloid precursor protein. *J. Biol. Chem.* **274,** 6483–6492 (1999).
12. Hsia, A. Y. Plaque-independent disruption of neural circuits in Alzheimer's disease mouse models. *Proc. Natl Acad. Sci. USA* **96,** 3228–3233 (1999).
13. Solomon, B., Koppel, R., Hanan, E. & Katzav, T. Monoclonal antibodies inhibit in vitro fibrillar aggregation of the Alzheimer β-amyloid peptide. *Proc. Natl Acad. Sci. USA* **93,** 452–455 (1996).
14. Lorenzo, A. & Yanker, B. A. β-amyloid neurotoxicity requires fibril formation and is inhibited by Congo red. *Proc. Natl Acad. Sci. USA* **91,** 12243–12247 (1994).
15. Walsh, D. M. *et al.* Amyloid β-protein fibrillogenesis. Structure and biological activity of protofibrillar intermediates. *J. Biol. Chem.* **274,** 25945–25952 (1999).
16. Hartley, D. M. Protofibrillar intermediates of amyloid β-protein induce acute electrophysiological changes and progressive neurotoxicity in cortical neurons. *J. Neurosci.* **19,** 8876–8884 (1999).
17. McLean, C. A. *et al.* Soluble pool of Aβ amyloid as a determinant of severity of neurodegeneration in Alzheimer's disease. *Ann. Neurol.* **46,** 860–866 (1999).
18. Naslund, J. *et al.* Correlation between elevated levels of amyloid β-peptide in the brain and cognitive decline. *J. Am. Med. Assoc.* **283,** 1571–1577 (2000).
19. Mucke, L. *et al.* High-level neuronal expression of Aβ1–42 in wild-type human amyloid protein precursor transgenic mice: synaptotoxicity without plaque formation. *J. Neurosci.* **20,** 4050–4058 (2000).
20. St George-Hyslop, P. & Westaway, D. Alzheimer's disease: antibody clears senile plaques. *Nature* **400,** 116–117 (1999).
21. Lu, D. C. A second cytotoxic proteolytic peptide derived from amyloid β-protein precursor. *Nature Med.* **6,** 397–404 (2000).
22. McLaurin, J., Franklin, T., Chakrabartty, A. & Fraser, P. E. Phosphatidylinositol and inositol involvement in Alzheimer amyloid-beta fibril growth and arrest. *J. Mol. Biol.* **278,** 183–194 (1998).
23. Janus, C. Spatial learning in transgenic mice expressing human presenilin 1 (PS1) transgenes. *Neurobiology of Aging* **21,** 541–549 (2000).
24. Cain, D. P., Beiko, J. & Boon, F. Navigation in the water maze: the role of proximal and visual cues, path intergration, and magnetic field information. *Psychobiology* **25,** 286–293 (1997).
25. Dudchenko, P. A., Goodridge, J. P., Seiterle, D. A. & Taube, J. S. Effects of repeated disorientation on the acquisition of spatial tasks in rats: dissociation between the appetetive radial arm maze and aversive water maze. *J. Exp. Psychol.* **23,** 194–210 (1997).
26. Gass, P. *et al.* Deficits in memory tasks of mice with CREB mutations depend on gene dosage. *Learn Mem.* **5,** 274–288 (1998).
27. Wehner, J. M., Sleight, S. & Upchurch, M. Hippocampal protein kinase C activity is reduced in poor spatial learners. *Brain Res.* **523,** 181–187 (1990).
28. Wisniewski, H. M., Wen, G. Y. & Kim, K. S. Comparison of four staining methods on the detection of neuritic plaques. *Acta Neuropathol.* **78,** 22–27 (1989).
29. Susuki, N. *et al.* An increased percentage of long amyloid B protein secreted by Familial Amyloid β Protein Precursor (BAPP717) mutants. *Science* **264,** 1336–1340 (1994).
30. Citron, M. *et al.* Mutant presenilins of Alzheimer's Disease increase production of 42 residue amyloid β-protein in both transfected cells and transgenic mice. *Nature Med.* **3,** 67–72 (1997).

Supplementary information is available on *Nature*'s World-Wide Web site (http://www.nature.com) or as paper copy from the London editorial office of *Nature*.

Acknowledgements

This work was supported by the Medical Research Council of Canada, Howard Hughes Medical Research Foundation, Alzheimer Society of Ontario, The W. Garfield Weston Foundation and the US National Institute of Aging. We thank G. Carlson for useful discussions, and R. Renlund, K. Parisien, J. Haight and J. Cowieson for help during mice immunization. None of the authors has a financial or other relationship with Elan Pharmaceuticals Inc.

Correspondence and requests for materials should be addressed to P.H.StG.-H. (e-mail: p.hyslop@utoronto.ca).

Aβ peptide vaccination prevents memory loss in an animal model of Alzheimer's disease

Dave Morgan*, David M. Diamond†‡, Paul E. Gottschall*, Kenneth E. Ugen§, Chad Dickey§, John Hardy‖, Karen Duff¶, Paul Jantzen*, Giovanni DiCarlo*, Donna Wilcock*, Karen Connor*, Jaime Hatcher#, Caroline Hope#, Marcia Gordon* & Gary W. Arendash#

** Alzheimer Research Laboratory, Department of Pharmacology, † Department of Psychology, § Department of Medical Microbiology and Immunology, # Alzheimer Research Laboratory, Department of Biology, University of South Florida, Tampa, Florida 33612, USA*
‡ James A. Haley VA Center, Tampa, Florida 33612, USA
‖ Department of Pharmacology, Mayo Clinic, Jacksonville, Florida 32224, USA
¶ Nathan Kline Institute, Orangeburg, New York 10962, USA

Vaccinations with amyloid-β peptide (AB) can dramatically reduce amyloid deposition in a transgenic mouse model of Alzheimer's disease[1]. To determine if the vaccinations had deleterious or beneficial functional consequences, we tested eight months of Aβ vaccination in a different transgenic model for

Alzheimer's disease in which mice develop learning deficits as amyloid accumulates[2,3] . Here we show that vaccination with Aβ protects transgenic mice from the learning and age-related memory deficits that normally occur in this mouse model for Alzheimer's disease. During testing for potential deleterious effects of the vaccine, all mice performed superbly on the radial-arm water-maze test of working memory. Later, at an age when untreated transgenic mice show memory deficits, the Aβ-vaccinated transgenic mice showed cognitive performance superior to that of the control transgenic mice and, ultimately, performed as well as nontransgenic mice. The Aβ-vaccinated mice also had a partial reduction in amyloid burden at the end of the study. This therapeutic approach may thus prevent and, possibly, treat Alzheimer's dementia.

The accumulation of fibrils formed from the Aβ peptide into amyloid plaques is a defining characteristic of Alzheimer's disease (AD). The Aβ vaccination protocol described in ref. 1 reduced Aβ deposits, which suggested that this approach might benefit AD patients. However, the functional consequences of such vaccinations might be deleterious. For example, plaque-associated inflammation promoted by the immunization could interfere with normal brain functioning, and/or lead to degenerative changes in the brain[4–8]. We used a novel working-memory task that combines elements of a radial-arm maze and a water maze. This radial-arm water maze is remarkably robust at detecting learning/memory deficits that develop in AD transgenic mice[2] and more efficient in sample size requirements than other memory tasks typically used for rodents[3].

To test the possibility that vaccinations might cause premature memory deficits in AD transgenic mice, we assessed learning/memory performance in the mice at 11.5 months of age after five inoculations with Aβ or the control vaccine, keyhole limpet haemocyanin (KLH). All mice showed strong learning and memory capacity, irrespective of treatment or transgene status (Fig. 1a). All groups averaged three to four errors on the first trial as they sought out the new platform location for that day, but averaged less than one error by trials 4 or 5, demonstrating intact working memory for platform location between trials and during the 30-min delay before trial 5. This strong performance by Aβ-vaccinated mice indicates that any inflammatory responses caused by the vaccine were not deleterious behaviourally.

Monthly inoculations were continued until the mice were 15.5 months, when these mice were tested again in the radial-arm water maze. At 15.5 months the KLH-vaccinated transgenic mice failed to demonstrate learning or memory of the platform location; their performance on all trials was the same (Fig. 1b). This is identical to the performance of other untreated transgenic mice that had been previously tested in this learning task at this age (Fig. 1c; ref. 3). In contrast, the Aβ-inoculated transgenic mice, although slower to learn platform location than nontransgenic mice on trial 3 (Fischer's least

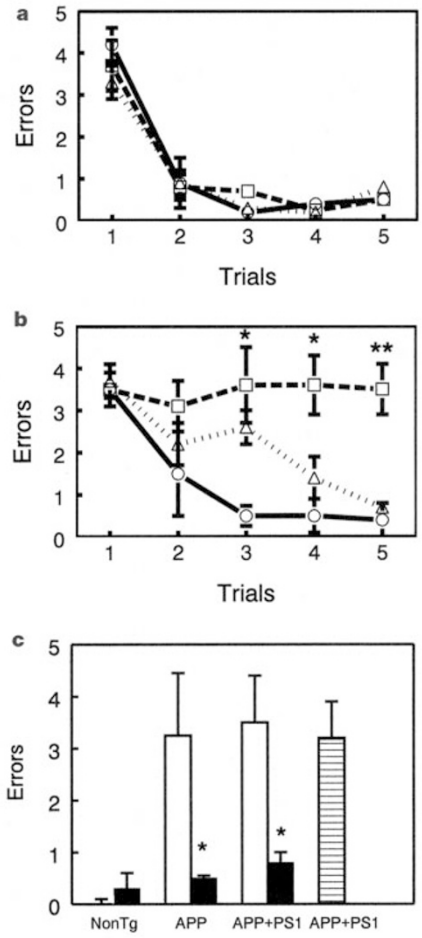

Figure 1 Radial-arm water-maze performance in vaccinated transgenic and nontransgenic mice. **a**, Nontransgenic mice (circles, solid lines), transgenic mice vaccinated with KLH (squares, dashed lines), and transgenic mice vaccinated with Aβ (triangles, dotted lines) were tested in the radial-arm water maze at 11.5 months of age (after five inoculations). All groups learned (trial 4) and remembered (trial 5) the platform location at this time point. In the same mice at 15.5 months of age (nine inoculations; **b**), the transgenic mice vaccinated with Aβ continued to show learning and memory of the platform location, whereas the transgenic mice vaccinated with KLH failed to show learning and memory for platform location on either trials 4 or 5 ($^{*}P < 0.05$, $^{**}P < 0.01$; KLH significantly different from other two groups by LSD post hoc analysis after MANOVA). This benefit of Aβ vaccination was found in both the APP-only and APP+PS1 transgenic mice (**c**), with significantly fewer errors on trial 5 in the Aβ-vaccinated groups (solid bars) than in the KLH-vaccinated group (open bars) of both genotypes ($^{*}P < 0.03$). Included for comparison is the trial 5 performance of another group (hatched bars) of untreated 15–16-month-old transgenic mice that were tested separately, and are reported on fully elsewhere[2].

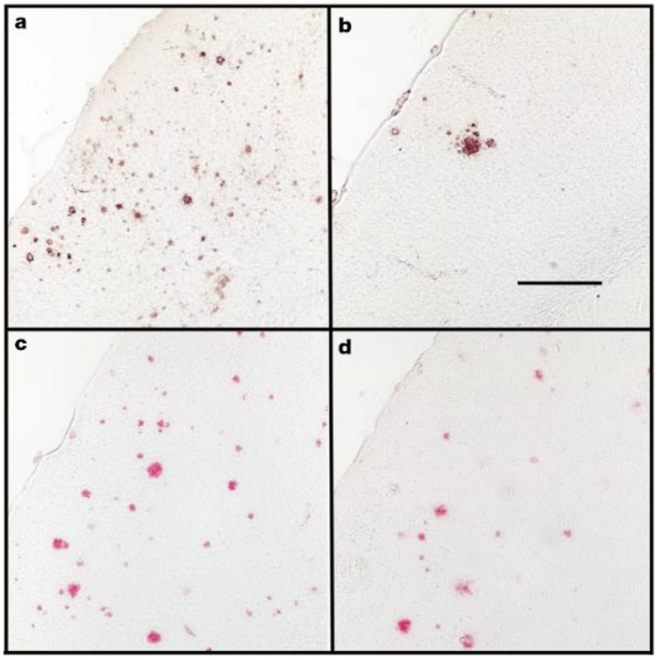

Figure 2 Amyloid pathology in transgenic mice vaccinated with KLH or Aβ. Immunohistochemistry for Aβ in frontal cortex is shown in (KLH-vaccinated) (**a**) and (Aβ-vaccinated) (**b**) in transgenic mice with values similar to the means shown in Fig. 3c. Congo-red staining is shown in (KLH) (**c**) and (Aβ) (**d**) in mice with values corresponding to the means in Fig. 3b. Horizontal sections are oriented with the corpus callosum in the lower right corner and anterior to the top. Scale bar, 500 μm.

significant difference (LSD), $P < 0.02$), were nearly flawless by trial 5, and performed significantly better than the KLH-vaccinated transgenic mice on both trials 4 and 5 (multiple analysis of variance, MANOVA: $F_{(2,15)} = 5.83$, $P < 0.02$ and $F_{(2,15)} = 12.16$, $P < 0.001$, respectively; KLH transgenic group different from both other groups by Fischer's LSD post hoc comparisons, $P < 0.05$ on trial 4 and $P < 0.01$ on trial 5). Our individual evaluation of the performance of the two transgenic genotypes made it clear that both APP-only and APP+PS1 transgenic mice benefited from the Aβ vaccinations (Fig. 1c).

Serological analysis indicated that mice injected with Aβ developed antibodies against the Aβ peptide. Very high titres were found in both transgenic and nontransgenic mice immunized with Aβ (IC_{50} = 27,000 ± 5,000 and 48,000 ± 18,000, respectively; not significant). There was no anti-Aβ activity in the KLH-immunized transgenic mice, untreated transgenic mice, nor nontransgenic mice at final dilutions of serum down to 1:16, indicating that transgenic mice did not spontaneously generate an antibody reaction to Aβ.

Immunization with Aβ caused a modest reduction in Aβ deposits in the frontal cortex, with a significant reduction in the Congo-red-stained area of APP+PS1 mice, and a significant reduction in the Aβ-immunostained area of APP mice (Fig. 2 and Fig. 3). Reductions of a similar extent were found in hippocampus. We also quantified immunostaining using Aβ40- and Aβ42-specific antisera, both of which exhibited the same modest reductions found in total Aβ immunostaining. We suspect that, with a larger sample size, statistically significant partial reductions would be found in all these measures consistent with other recent reports[9–11]. In general, the percentage reduction in Aβ deposition was greater in the APP mice than the APP+PS1 mice. The absolute reductions were greater, however, in the doubly transgenic animals. The APP+PS1 mice already had substantial Aβ deposits by the time vaccinations were initiated[12]. Further studies will test whether beginning vaccinations at an earlier age, or combining vaccination with other Aβ-lowering treatments, will result in more complete protection from Aβ deposition, and improve the cognitive performance of 15-months-old transgenic mice even further.

Our most important finding here is that Aβ vaccination protects transgenic mice from developing memory deficits compared with KLH-immunized (control) transgenic mice. But how important is the learning paradigm in discerning these differences. We have found that in using the reference-memory version of the water maze, mice of this age (15.5 months) have deficits in escape latency, but not retention on the probe trial[3]. Thus, the more demanding working-memory version of the water-maze task may be essential to detect such differences. Similarly, a spatial task would require intact function of hippocampal and, to a lesser extent, cortical structures, the locations where plaques accumulate earliest and to the greatest extent in these mice[12–14].

This vaccination-associated protection from memory impairment occurs in the presence of reduced, but still substantial Aβ deposits. The mechanism by which immunization with Aβ blocks learning and memory deficits is not understood. One possibility is that the antibodies neutralize Aβ in some restricted compartment or deplete a non-deposited form of Aβ (for example, a soluble form) that is responsible for the memory loss observed. Recently, soluble Aβ has been proposed as the cause of synapse loss in APP transgenic mice, as some transgenic lines develop reductions in synaptophysin immunoreactivity in dentate gyrus without developing Aβ deposits[15]. A second possibility is that microglia activated by the inoculations[1] can clear the deposited Aβ, thereby permitting normal cognitive function. This is not easily reconciled with the relatively modest Aβ clearance detected, although exhaustive regional analyses have yet to be completed. Perhaps even mice that have already developed extensive brain pathology and memory deficits can benefit from vaccinations given later in life. In view of the absence of adverse effects on behaviour and brain functioning, and the protection of memory functions by the Aβ vaccines, we strongly recommend testing of this and related approaches for the treatment and prevention of Alzheimer's disease. □

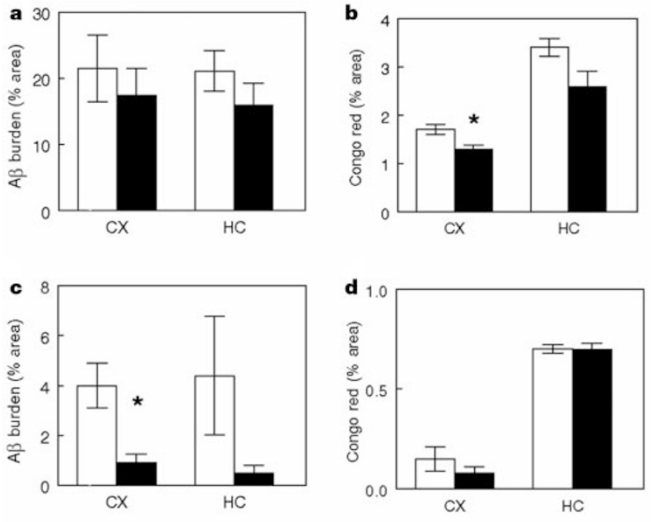

Figure 3 Measurement of amyloid histopathology after Aβ peptide immunization. **a**, **b**, Results for the APP+PS1 mice; **c**, **d**, results for APP-only transgenic mice. A significant reduction in Congo-red staining in frontal cortex was found in APP+PS1 mice vaccinated with Aβ ($n = 4$) compared to in APP+PS1 mice vaccinated with KLH ($n = 5$; **b**). There was a significant reduction in Aβ immunostaining in APP-only transgenic mice vaccinated with Aβ ($n = 3$) compared to in KLH-vaccinated APP mice ($n = 2$; **c**). *, $P < 0.05$; **, $P < 0.01$ by *t*-test. CX, frontal cortex; HC, hippocampus.

Methods

Vaccination protocols

Mice were obtained by breeding Tg 2576 APP transgenic mice[16] with PS1 line 5.1 transgenic mice[17], resulting in nontransgenic, APP, APP+PS1 and PS1 transgenic mice as described by us previously[12,13]. Human Aβ1–42 peptide (Bachem) was suspended in pyrogen-free Type I water at 2.2 mg ml^{-1} then mixed with 10 × PBS to yield 1 × PBS and incubated overnight at 37 °C. Control mice were injected with KLH that was prepared in the same manner. The antigen suspension was mixed 1:1 with Freund's complete adjuvant and 100 μg Aβ injected subcutaneously by an experimenter who had no role in the behavioural testing. A boost of the same material (prepared freshly) was made in incomplete Freund's at two weeks and injected once monthly for the next three months. Subsequent monthly boosts were made in mineral oil. Mice were vaccinated, beginning at 7.5 months of age. The sample size of each group was: 6 (3 female/3 male) nontransgenic mice vaccinated with Aβ or KLH; 7 (4 female/3 male) transgenic mice vaccinated with Aβ; 7 (4 female/3 male) transgenic mice vaccinated with KLH. The first post-vaccination behavioural testing period was started 5 days after the fifth vaccination at 11.5 months of age. The second behavioural testing period was started at 15.5 months of age, one month after the ninth vaccination. Mice were killed at 16 months of age. We note that transgenic and nontransgenic mice were also tested for performance in the radial-arm water maze at 6 months of age (before vaccination) and all mice performed well.

Radial-arm water maze testing

Experimenters were unaware of the experimental conditions of the mice at the time of testing. The maze consisted of a circular pool 1 m in diameter with six swim alleys (arms) 19 cm wide that radiated out from an open central area (40 cm in diameter), with a submerged escape platform located at the end of one of the arms[3,18]. Spatial cues were present on the walls and ceiling of the testing room. The escape platform was placed in a different arm each day, forcing mice to use working memory to solve the task. Each day, mice were given the opportunity to learn the location of the submerged platform during four consecutive acquisition trials followed 30 min later by a retention trial (trial 5). On each trial, the mouse was started in one arm not containing the platform and allowed to swim for up to one minute to find the escape platform. Upon entering (all four paws within the swim alley) an incorrect arm or failing to select an arm after 20 s, the mouse was gently pulled back to the start arm for that trial and charged an error. All mice spent 30 s on the platform following each trial before beginning the next trial. On subsequent trials that day, the start arm was varied, so the mouse could not simply learn the motor rule 'second arm to the left', but must learn the spatial location of the platform that day. After the fourth trial was completed, the mice were placed in their home cage for 30 min, then returned to the maze and administered the retention trial. The platform was located in the same arm on each trial within a day, and was in a different arm across days. Over 1–2 weeks of

training, control groups gradually improved performance as they learned the procedural aspects of the task, reaching an asymptotic level of 0.5–1 errors on trials 4 and 5. In the experiments presented here mice were trained until the nontransgenic mice reached asymptotic performance: 9 days at 11.5 months or 11 days at 15.5 months. The scores for each mouse on the last two days of testing were averaged and used for statistical analysis. Sensorimotor tests identified no differences among these groups in open field behaviour or string agility testing. As in earlier work, all transgenic mice were impaired on the balance beam, a deficit observed as early as six months of age[3], but this deficit was not modified by Aβ vaccination.

ELISA analysis for serum antibodies

Ninety-six-well Immulon 4HBX (Dynex) micro plates were coated with the Aβ1–42 protein (250 ng per well) for 1 h at 37 °C. They were washed four times with 0.45% NaCl + 0.05% Tween-20 (washing buffer, WB). The plates were blocked with 5% non-fat dry milk (NFDM) in PBS overnight at 4 °C and washed the following day. Mouse serum was prepared in PBS at an initial dilution of 1:16 and subsequent twofold dilutions were made. All samples were run in duplicate and incubated at 37 °C for 1 h followed by washing 10 times in WB. Plates were blocked a second time with 5% NFDM in PBS for 30 min at 37 °C followed by washing five times before the addition of an anti-mouse IgG HRP-conjugate. The secondary antibody was diluted 1:5,000 in PBS and incubated for 1 h at 37 °C. Plates were then washed 10 times in WB and developed with 3,3,5,5-tetramethylbenzidine substrate (Sigma) in perborate buffer (Sigma). The reaction was stopped with 2 M sulphuric acid. Plates were read spectrophotometrically at 450 nm. The anti-Aβ1–42 antibody titre was defined as the reciprocal of the dilution of antisera that produced 50% of the maximum signal detected for that sample.

Histopathology

Mice were overdosed with pentobarbital, perfused with saline and their brains removed. One hemisphere was immersion-fixed in fresh, buffered paraformaldehyde for 24 h. Frozen sections were stained for Aβ peptides by immunohistochemistry[13,19] or for Congo red. The area of frontal cortex occupied by stain was measured with a Videometric V150 image analysis system (Oncor) on a Nikon Microphot FX microscope. Stained regions were measured using HSI segmentation by an experimenter unaware of the subject condition. Both stain intensity and area were measured, although only areas are reported here as this is the convention for Aβ deposits ('amyloid burden'). The results were not qualitatively different when evaluating area, stain intensity or their product (total immunoreactivity[19]). Data were collected from equally spaced horizontal sections for both frontal cortex (anterior to the corpus callosum; 12 per mouse) and hippocampus (10 per mouse).

Received 21 August; accepted 7 November 2000.

1. Schenk, D. *et al.* Immunization with amyloid-beta attenuates Alzheimer-disease-like pathology in the PDAPP mouse. *Nature* **400,** 173–177 (1999).
2. Gordon, M. N. *et al.* Correlation between cognitive deficits and Aβ deposits in transgenic APP+PS1 mice. *Neurobiol. Aging* (in the press).
3. Arendash, G. W. *et al.* Progressive behavioral impairments in transgenic mice carrying both mutant APP and PS1 transgenes. *Brain Res.* (in the press).
4. McGeer, E. G. & McGeer, P. L. The importance of inflammatory mechanisms in Alzheimer disease. *Exp. Gerontol.* **33,** 371–378 (1998).
5. Rogers, J. *et al.* Inflammation and Alzheimer's disease pathogenesis. *Neurobiol. Aging* **17,** 681–686 (1996).
6. Frautschy, S. A. Microglial response to amyloid plaques in APPsw transgenic mice. *Am. J. Pathol.* **152,** 307–317 (1998).
7. Masliah, E. *et al.* Comparison of neurodegenerative pathology in transgenic mice overexpressing V717F beta-amyloid precursor protein and Alzheimer's disease. *J. Neurosci.* **16,** 5795–5811 (1996).
8. Calhoun, M. E. *et al.* Neuron loss in APP transgenic mice. *Nature* **395,** 755–756 (1998).
9. Weiner, H. L. *et al.* Nasal administration of amyloid-beta peptide decreases cerebral amyloid burden in a mouse model of Alzheimer's disease. *Ann. Neurol.* **48,** 567–579 (2000).
10. Bard, F. *et al.* Peripherally administered antibodies against amyloid beta-peptide enter the central nervous system and reduce pathology in a mouse model of Alzheimer disease. *Nature Med.* **6,** 916–919 (2000).
11. Frenkel, D., Solomon, B. & Benhar, I. Modulation of Alzheimer's beta-amyloid neurotoxicity by site-directed single-chain antibody. *J. Neuroimmunol.* **106,** 23–31 (2000).
12. Holcomb, L. *et al.* Accelerated Alzheimer-type phenotype in transgenic mice carrying both mutant amyloid precursor protein and presenilin 1 transgenes. *Nature Med.* **4,** 97–100 (1998).
13. Holcomb, L. A. *et al.* Behavioral changes in transgenic mice expressing both amyloid precursor protein and presenilin-1 mutations: Lack of association with amyloid deposits. *Behav. Gen.* **29,** 177–185 (1999).
14. McGowan, E. *et al.* Amyloid phenotype characterization of transgenic mice overexpressing both mutant amyloid precursor protein and mutant presenilin 1 transgenes. *Neurobiol. Dis.* **6,** 231–244 (1999).
15. Mucke, L. *et al.* High level neuronal expression of Aβ1–42 in wild-type human amyloid precursor protein transgenic mice: Synaptotoxicity without plaque formation. *J. Neurosci.* **20,** 4050–4058 (2000).
16. Hsiao, K. *et al.* Correlative memory deficits, Abeta elevation, and amyloid plaques in transgenic mice. *Science* **274,** 99–102 (1996).
17. Duff, K. *et al.* Increased amyloid-beta42(43) in brains of mice expressing mutant presenilin 1. *Nature* **383,** 710–713 (1996).
18. Diamond, D. M., Park, C. R., Heman, K. L. & Rose, G. M. Exposing rats to a predator impairs spatial working memory in the radial arm water maze. *Hippocampus* **9,** 542–551 (1999).
19. Gordon, M. N., Schreier, W. A., Ou, X., Holcomb, L. A. & Morgan, D. G. Exaggerated astrocyte reactivity after nigrostriatal deafferentation in the aged rat. *J. Comp. Neurol.* **388,** 106–119 (1997).

Acknowledgements

We thank K. Hsiao-Ashe for sharing the Tg2576 mouse line. We thank R. Engelman and U. Owens for superb veterinary services in the maintenance of the transgenic colony. We thank I. Johnson for accounting services associated with the project. This work was supported by grants from the National Institute on Aging to M.G. and D.M., from the National Institute of Allergy and Infectious Disease and the National Heart Lung and Blood Institute to K.U., by the Benjamin Research Trust to D.M. and by an award from the University of South Florida Research Foundation.

Correspondence and requests for materials should be addressed to D. M. (e-mail: dmorgan@hsc.usf.edu).

Induction of vanilloid receptor channel activity by protein kinase C

Louis S. Premkumar & Gerard P. Ahern

Department of Pharmacology, Southern Illinois University School of Medicine, Springfield, Illinois 62702, USA

Capsaicin or vanilloid receptors (VRs) participate in the sensation of thermal and inflammatory pain[1–3]. The cloned (VR1) and native VRs are non-selective cation channels directly activated by harmful heat, extracellular protons and vanilloid compounds[4–8]. However, considerable attention has been focused on identifying other signalling pathways in VR activation; it is known that VR1 is also expressed in non-sensory tissue[1,9] and may mediate inflammatory rather than acute thermal pain[3]. Here we show that activation of protein kinase C (PKC) induces VR1 channel activity at room temperature in the absence of any other agonist. We also observed this effect in native VRs from sensory neurons, and phorbol esters induced a vanilloid-sensitive Ca^{2+} rise in these cells. Moreover, the pro-inflammatory peptide, bradykinin, and the putative endogenous ligand, anandamide, respectively induced and enhanced VR activity, in a PKC-dependent manner. These results suggest that PKC may link a range of stimuli to the activation of VRs.

PKC is a prominent participant in pain signalling. Targeted deletion of PKC-ϵ in mice[10] markedly attenuates thermal- and acid-induced hyperalgesia. In turn, activation of PKC-ϵ potentiates heat-evoked currents in sensory neurons[11,12]. Further, the algesic peptide, bradykinin, potentiates heat responses[11,12], induces depolarization[13–16], and evokes secretion[17–19] from vanilloid-sensitive neurons in a PKC-dependent manner. However, the molecular targets for these effects have not yet been clearly identified. We therefore investigated whether these actions of PKC are mediated by VRs. Rat VR1 was expressed in *Xenopus laevis* oocytes and studied using a two-electrode voltage clamp technique. Treatment with 12-*O*-tetradecanoylphorbol-13-acetate (TPA) to activate endogenous PKC increased the amplitude of currents evoked by capsaicin (Fig. 1a, c), anandamide (Fig. 1b, c) and protons (extracellular pH 5; data not shown). In addition, TPA by itself produced a slowly developing current (Fig. 1a, b) that was not observed in uninjected oocytes ($n = 5$) or oocytes expressing the NMDA (*N*-methyl D-aspartate) receptor ($n = 8$). These actions were probably mediated by PKC because no responses were elicited by the inactive TPA analogue, 4α-phorbol ($n = 4$), and responses to TPA were inhibited by the selective PKC inhibitor[20], bisindolylmaleimide (BIM, 200 nM, Fig. 1c).

Next, we examined whether the current induced by TPA alone was mediated by VR1. In these experiments VR1-expressing oocytes were treated separately with either TPA or capsaicin, to avoid cross-sensitization. Figure 1d shows the response of a TPA-treated oocyte to a series of depolarizing pulses from −80 mV to +80 mV. Outwardly rectified currents were evoked that were similar to those

with either the solution listed above (without ascorbic acid, *myo*-inositol, and Na-pyruvate) or a HEPES-based solution containing (in mM) 145 NaCl, 25 glucose, 2.5 KCl, 1 $MgCl_2$, 2 $CaCl_2$, 10 HEPES, bubbled with O_2 (used for Fig. 3a–c). During spillover experiments, the extracellular solution also contained 60 nM CGP54626 to prevent activation of $GABA_B$ receptors. Presynaptic terminals were labelled with lucifer yellow and visually identified as a calyx.

Electrodes for postsynaptic recording had resistances of 2–3 MΩ; series resistances during recordings were <5 MΩ, compensated electronically by 90%. Pre- and postsynaptic cells were voltage clamped to −60 mV, unless otherwise indicated. For presynaptic recordings, electrodes were 5–6 MΩ, with series resistances of 10–25 MΩ, compensated by 80–90%. Pipettes for recording EPSCs contained (in mM) 135 CsF, 5 CsCl, 5 EGTA, 10 HEPES and 2 QX314 (*N*-(2,6-dimethylphenylcarbamoylmethyl) triethylammonium chloride) (286 mOsm) at pH 7.25 with CsOH. Pipettes for pre- and postsynaptic recording of glycine responses contained either low $[Cl^-]_i$ solution (in mM): 125 Cs-methane sulphonate, 15 CsCl, 5 EGTA, 1 $MgCl_2$, 10 HEPES, 0.2 lucifer yellow (290 mOsm) at pH 7.2 with CsOH, or high-$[Cl^-]_i$ solution in which Cs-methane sulphonate was replaced with CsCl. Current-clamp recording from gramicidin-perforated patches was made with pipettes filled with high-$[Cl^-]_i$ solution where KCl replaced Cs-methane sulphonate and CsCl. For paired pre- and postsynaptic recordings, presynaptic pipettes contained (in mM) 150 KCl (or 145 K-gluconate and 5 KCl for low-$[Cl^-]_i$ solution), 0.2 EGTA, 1 $MgCl_2$ and 10 HEPES[13]. During simultaneous pre- and postsynaptic recordings, no rundown of EPSCs was observed over the 10–15 min necessary for the experiment. Voltages were corrected for junction potentials.

EPSCs and IPSCs were elicited by voltage pulses (100 μs, 10–20 V stimuli) delivered through a glass pipette. During paired pre- and postsynaptic recording, EPSCs were evoked by action potentials elicited by a depolarizing current pulse delivered through the presynaptic recording electrode. mEPSCs were recorded at −60 mV in the presence of 0.5 μM TTX. Drugs were applied by pressure ejection or by bath perfusion. Gramicidin D was prepared in methanol at 5 mg ml^{-1} and then dissolved in intracellular solution to a final concentration of 5 μg ml^{-1}. EGTA-AM prepared as a stock solution in dimethyl sulphoxide (DMSO) just before the experiment was diluted in bath solution to 0.2 mM (final concentration of DMSO, 0.1%). For Ca^{2+} measurements, voltage-clamped terminals were loaded with the presynaptic K-gluconate pipette fill containing 20 μM Oregon Green 488 BAPTA-1, and without Mg^{2+}. Dye was excited (Hg lamp with 1% neutral density filter, 470-nm bandpass excitation filter) at 1 Hz for 100 ms to minimize bleaching. Fluorescence emission (535 nm bandpass) was detected with a photomultiplier tube and was restricted to a region just larger than the cell body diameter. Background values, measured in a region of identical size adjacent to cell body, were subtracted and fluorescence changes normalized for the average pre-stimulus intensity ($\Delta F/F_0$). Statistical significance was established using paired and unpaired *t*-tests, as indicated, and errors reported as ±1 s.d.

Received 24 November 2000; accepted 27 March 2001.

1. Eccles, J. C., Schmidt, R. F. & Willis, W. D. Pharmacological studies of presynaptic inhibition. *J. Physiol.* **168,** 500–530 (1963).
2. Tachibana, M. & Kaneko, A. γ-Aminobutyric acid exerts a local inhibitory action on the axon terminal of bipolar cells: evidence for negative feedback from amacrine cells. *Proc. Natl Acad. Sci. USA* **84,** 3501–3505 (1987).
3. Zhang, S. J. & Jackson, M. B. $GABA_A$ receptor activation and the excitability of nerve terminals in the rat posterior pituitary. *J. Physiol. (Lond.)* **483,** 583–595 (1995).
4. Pouzat, C. & Marty, A. Somatic recording of GABAergic autoreceptor current in cerebellar stellate and basket cells. *J. Neurosci.* **19,** 1675–1690 (1999).
5. Forsythe, I. D. & Barnes-Davies, M. The binaural auditory pathway: excitatory amino acid receptors mediate dual timecourse excitatory postsynaptic currents in the rat medial nucleus of the trapezoid body. *Proc. R. Soc. Lond. B.* **25,** 151–157 (1993).
6. Taschenberger, H. & von Gersdorff, H. Fine tuning an auditory synapses for speed and fidelity during a critical developmental period. *J. Neurosci.* **24,** 9162–9173 (2000).
7. Bormann, J., Hamill, O. P. & Sakmann, B. Mechanism of anion permeation through channels gated by glycine and gamma-aminobutyric acid in mouse cultured spinal neurones. *J. Physiol. (Lond.)* **385,** 243–286 (1987).
8. Isaacson, J. S. $GABA_B$ receptor-mediated modulation of presynaptic currents and excitatory transmission at a fast central synapse. *J. Neurophysiol.* **80,** 1571–1576 (1998).
9. Takahashi, T., Kajikawa, Y. & Tsujimoto, T. G-Protein-coupled modulation of presynaptic calcium currents and transmitter release by a $GABA_B$ receptor. *J. Neurosci.* **18,** 3138–3146 (1998).
10. Martin, A. R. In *Handbook of Physiology, Sec. I, The Nervous System* (eds Brookhard, J. M., Mountscastle, V. B., Kandel, E. R. & Geiger, S. R.) 329–356 (Am. Physiol. Soc., Bethesda, 1977).
11. Atluri, P. P. & Regehr, W. G. Delayed release of neurotransmitter from cerebellar granule cells. *J. Neurosci.* **18,** 8214–8227 (1998).
12. Wang, L. Y. & Kaczmarek, L. K. High-frequency firing helps replenish the readily releasable pool of synaptic vesicles. *Nature* **394,** 384–388 (1998).
13. Borst, J. G. & Sakmann, B. Calcium influx and transmitter release in a fast CNS synapse. *Nature* **383,** 431–434 (1996).
14. Akaike, N. Gramicidin perforated patch recording and intracellular chloride activity in excitable cells. *Prog. Biophys. Mol. Biol.* **65,** 251–264 (1996).
15. Tachibana, M., Okada, T., Arimura, T., Kobayashi, K. & Piccolino, M. Dihydropyridine-sensitive calcium current mediates neurotransmitter release from bipolar cells of the goldfish retina. *J. Neurosci.* **13,** 2898–2909 (1993).
16. Cuttle, M. F., Tsujimoto, T., Forsythe, I. D. & Takahashi, T. Facilitation of the presynaptic calcium current at an auditory synapse in rat brainstem. *J. Physiol. (Lond.)* **512,** 723–729 (1998).
17. Borst, J. G. & Sakmann, B. Facilitation of presynaptic calcium currents in the rat brainstem. *J. Physiol. (Lond.)* **513,** 149–155 (1998).
18. Isaacson, J. S., Solis, J. M. & Nicoll, R. A. Local and diffuse synaptic actions of GABA in the hippocampus. *Neuron* **10,** 165–175 (1993).
19. Dittman, J. S. & Regehr, W. G. Mechanism and kinetics of heterosynaptic depression at a cerebellar synapse. *J. Neurosci.* **17,** 9048–9059 (1997).
20. Min, M. Y., Rusakov, D. A. & Kullmann, D. M. Activation of AMPA, kainate, and metabotropic receptors at hippocampal mossy fiber synapses: role of glutamate diffusion. *Neuron* **21,** 561–570 (1998).
21. Mitchell, S. J. & Silver, R. A. Glutamate spillover suppresses inhibition by activating presynaptic mGluRs. *Nature* **404,** 498–502 (2000).
22. Banks, M. I. & Smith, P. H. Intracellular recordings from neurobiotin-labeled cells in brain slices of the rat medial nucleus of the trapezoid body. *J. Neurosci.* **12,** 2819–2837 (1992).
23. Wu, S. H. & Kelly, J. B. Synaptic pharmacology of the superior olivary complex studied in mouse brain slice. *J. Neurosci.* **12,** 3084–3097 (1992).
24. Grothe, B. & Sanes, D. H. Synaptic inhibition influences the temporal coding properties of medial superior olivary neurons: an in vitro study. *J. Neurosci.* **14,** 1701–1709 (1994).
25. Funabiki, K., Koyano, K. & Ohmori, H. The role of GABAergic inputs for coincidence detection in the neurones of nucleus laminaris of the chick. *J. Physiol. (Lond.)* **508,** 851–869 (1998).
26. Schneggenburger, R. & Neher, E. Intracellular calcium dependence of transmitter release rates at a fast central synapse. *Nature* **406,** 889–893 (2000).
27. Bollmann, J. H., Sakmann, B. & Borst, J. G. Calcium sensitivity of glutamate release in a calyx-type terminal. *Science* **289,** 953–957 (2000).

Supplementary information is available on *Nature*'s World-Wide Web site (http://www.nature.com) or as paper copy from the London editorial office of *Nature*.

Acknowledgements

We thank S. Brenowitz, H. von Gersdorff and C. Jahr for comments on the manuscript. Supported by NIH grants and a Fogarty International Center Fellowship.

Correspondence and requests for materials should be addressed to L.T. (e-mail: trussell@ohsu.edu).

LTRPC7 is a Mg·ATP-regulated divalent cation channel required for cell viability

Monica J. S. Nadler*†, Meredith C. Hermosura*‡, Kazunori Inabe*§, Anne-Laure Perraud*†, Qiqin Zhu†, Alexander J. Stokes†, Tomohiro Kurosaki§, Jean-Pierre Kinet†, Reinhold Penner‡, Andrew M. Scharenberg†‖ & Andrea Fleig‡

† *Department of Pathology, Beth Israel Deaconess Medical Center and Harvard Medical School, Boston, Massachusetts 02215, USA*
‡ *Laboratory of Cell and Molecular Signaling, Center for Biomedical Research at The Queen's Medical Center and John A. Burns School of Medicine at the University of Hawaii, Honolulu, Hawaii 96813, USA*
§ *Department of Molecular Genetics, Institute for Liver Research, Kansai Medical University, Osaka 570-8506, Japan*
* *These authors contributed equally to this work*

The molecular mechanisms that regulate basal or background entry of divalent cations into mammalian cells are poorly understood. Here we describe the cloning and functional characterization of a Ca^{2+}- and Mg^{2+}-permeable divalent cation channel, LTRPC7 (nomenclature compatible with that proposed in ref. 1), a new member of the LTRPC family of putative ion channels. Targeted deletion of LTRPC7 in DT-40 B cells was lethal, indicating that LTRPC7 has a fundamental and nonredundant role in cellular physiology. Electrophysiological analysis of HEK-293 cells overexpressing recombinant LTRPC7 showed large currents regulated by millimolar levels of intracellular Mg·ATP and Mg·GTP with the permeation properties of a voltage-independent divalent cation influx pathway. Analysis of several cultured cell types demonstrated small magnesium-nucleotide-regulated metal ion currents (MagNuM) with regulation and permeation properties essentially identical to the large currents observed in cells expressing recombinant LTRPC7. Our data indicate that LTRPC7, by

‖ Present address: Department of Pediatrics and Immunology, University of Washington and Children's Hospital and Medical Center, Seattle, Washington 98195-6320, USA.

virtue of its sensitivity to physiological Mg·ATP levels, may be involved in a fundamental process that adjusts plasma membrane divalent cation fluxes according to the metabolic state of the cell.

As part of a systematic effort to identify novel Ca^{2+}/cation channels expressed in haematopoietic cells, we cloned a putative cation channel transcript, which we later designated LTRPC7. The predicted protein encoded by the LTRPC7 transcript is homologous to other LTRPC family members throughout its first 1,200 amino acids (Fig. 1a), but is notable for its ubiquitous distribution (see Supplementary Information) and for a long and unique carboxy-terminal tail that contains a domain of significant homology to the MHCK/EEF2α family of protein kinases[2] (Fig. 1a).

To investigate LTRPC7's role in cell physiology, we used the DT-40 B-cell system to produce a cell line with targeted deletion of its LTRPC7 genes. Although targeted deletion of one LTRPC7 allele was easily obtained, no clones were obtained with targeted integrations into both alleles (data not shown), indicating that LTRPC7 is required for cellular viability. We therefore took an inducible deletion approach (Fig. 1b) by producing a viable DT-40 cell line that expressed a tamoxifen-controlled Cre recombinase, and which also had a stable targeted deletion of one LTRPC7 allele and LoxP sites bracketing the LTRPC7 exons encoding transmembrane span 5, the putative channel pore region and transmembrane span 6 in the other LTRPC7 allele. Activation of the Cre recombinase by treatment of this cell line with tamoxifen induced the deletion of these three exons in most cells (Fig. 1c). As shown in Fig. 1d, this induced the growth arrest and subsequent death of the cells over a 48–72-h time frame, providing strong evidence that LTRPC7 is fundamental in cellular function.

For electrophysiological analysis of LTRPC7, we produced HEK-293 cell lines with tetracycline-controlled expression of a Flag-tagged LTRPC7 construct. Treatment of these cells with tetracycline for 24 h induced a Flag-reactive band with a relative molecular mass of 220,000 (M_r 220K; predicted size of Flag–LTRPC7, Fig. 2a). However, by 72–96 h, LTRPC7-expressing cells began to swell, detach and die (Fig. 2b, similar results for all clones). Because of the potential for cell toxicity at times greater than 24 h after induction, all subsequent analyses were performed 18–24 h after induction. In this time frame, induced cells developed large whole-cell currents over a 100–300-s time period (Fig. 2c) with a characteristic outwardly rectifying current–voltage relationship (Fig. 2d) when perfused with Cs^+-based internal solutions (identical results were obtained with K^+, data not shown). With choline-based intracellular solutions, the large outward conductances were significantly suppressed, indicating that outward currents through LTRPC7 are carried by cations. Stationary noise analysis of outward currents was performed at +60 mV in the frequency range 0.001–1 kHz and revealed characteristic increases in current variance during activation of the whole-cell current that levelled off and finally decreased as the current was fully activated. Through linear regression of variance versus mean current during the initial activation phase, we determined an average slope of 2.5 ± 0.4 pA (n = 4), corresponding to a single-channel conductance of ~40 pS, based on a reversal potential of 0 mV. Because mono- and divalent ions do not permeate LTRPC7 independently of each other (see below), this value applies in a strict manner only to the test potential of +60 mV and the ionic conditions imposed by our external and internal solutions.

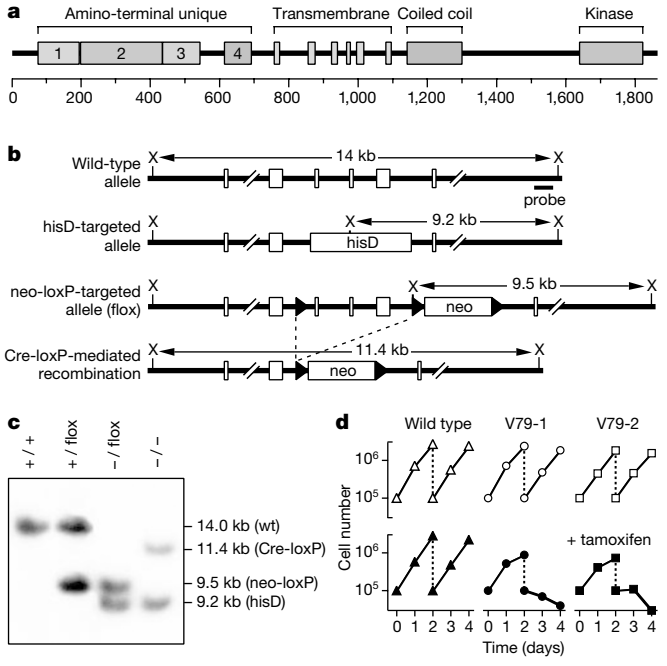

Figure 1 LTRPC7 structure and inducible knockout of LTRPC7 in the chicken B-cell line DT-40. **a**, Schematic of LTRPC7 with amino-terminal unique regions 1–4, transmembrane domain regions, coiled-coil region and the MHCK/EEF2α kinase homology domain (kinase). **b**, Schematics of wild-type and mutated DT-40 LTRPC7 alleles. Restriction enzyme sites (X, *Xba*I), probe for Southern blot analysis (solid bar), exons (open rectangle) and loxP sites (solid triangle) are indicated. Three exons, including part of the putative transmembrane region (corresponding to mouse LTRPC7 amino-acid residues 997–1,158), were replaced with *hisD* cassettes in the *hisD*-targeted allele and flanked by two *loxP* sequences in the *neo-loxP*-targeted allele. *Xba*I fragments detected by the probe are shown for wild-type and mutated alleles. **c**, Southern blot analysis of *Xba*I-digested DNA from wild-type and mutant DT-40 cells. **d**, Effect of LTRPC7 inactivation on cell proliferation. DT-40 wild type and mutant clones (V79-1 and V79-2) harbouring *hisD*- and *neo-loxP*-targeted alleles were cultured either without (open symbols) or with (filled symbols) 200 nM tamoxifen. Cell numbers were adjusted to 1×10^5 cells per ml, 2 days after cultivation. Viable cells were monitored daily by trypan blue exclusion.

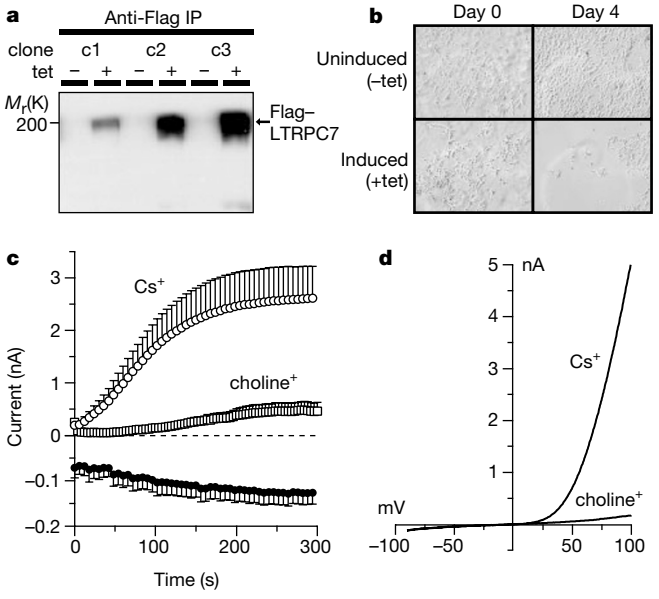

Figure 2 Functional expression of LTRPC7 as a cation channel**. a**, SDS–polyacrilamide gel electrophoresis (PAGE) analysis of three clonal HEK-293 cell lines (c1–c3) expressing a tetracycline-controlled Flag–LTRPC7 construct. Anti-Flag immunoreactive proteins before (left lanes) or after 24 h of tetracycline (right lanes). **b**, Phase contrast images of representative patches of LTRPC7-overexpressing HEK-293 cells 0 and 4 days after treatment with or without tetracycline. **c**, Average inward and outward currents carried by LTRPC7 at –80 and +80 mV, respectively. Cells perfused with ATP-free Cs^+-glutamate internal solution (n = 7, ± s.e.m.). Outward current was markedly suppressed when choline was used as the major internal cation, with only 10 mM Cs^+ present (n = 3, ± s.e.m.). **d**, Current–voltage relationships under experimental conditions as in **c**, obtained from representative cells 200 s after whole-cell establishment.

We next analysed the permeation characteristics of LTRPC7-mediated currents (Fig. 3). Inward currents were not affected by substitution of choline for Na^+ and K^+ in the extracellular solution (Fig. 3a), indicating that the inward current is carried exclusively by divalent ions. Furthermore, inward currents are not affected by removal of either Ca^{2+} or Mg^{2+} alone (Fig. 3b, c). Only the complete removal of external divalents amplifies both inward and outward monovalent current flow (Fig. 3d). The current–voltage relationship under divalent-free conditions (Fig. 3e) demonstrates linearization of the outward currents and significant enhancement of inward currents as compared with the divalent-containing situation. These effects are probably due to relief from permeation block by the divalent ions, which is expected to be strongest at negative potentials and gradually decreases as the reversal potential for divalent ions is approached.

The above data are most simply explained by a model in which the LTRPC7 pore has a high affinity for and is permeant to $Ca^{2+}$and Mg^{2+}, which accordingly obstruct inward fluxes of monovalent cations. Consistent with this model, LTRPC7-dependent inward currents are enhanced and outward currents suppressed when cells are exposed to isotonic (120 mM) $CaCl_2$ and $MgCl_2$ solutions, conditions in which Ca^{2+} or Mg^{2+} are the only available cationic charge carriers (Fig. 3f and g, respectively). In light of the significant Mg^{2+} permeation of LTRPC7, a feature to our knowledge unprecedented among known ion channels, we assessed Mg^{2+} permeation at different extracellular Mg^{2+} concentrations in reference to inward currents carried by 2 mM Mg^{2+} (Fig. 3h; note the absence of external Ca^{2+}). Higher concentrations of Mg^{2+} increased inward currents carried by Mg^{2+} and submillimolar Mg^{2+} concentrations progressively increased monovalent influx until divalent-free medium gave rise to large monovalent inward currents. Thus, LTRPC7 exhibits clear Mg^{2+}-dependent anomalous mole fraction behaviour. At the same time, outward currents are inhibited with increasing Mg^{2+} concentrations (Fig. 3i), probably in part owing to the shift in reversal potential occurring with the increase in extracellular Mg^{2+} concentrations, but also indicating that Mg^{2+} upon permeation might suppress LTRPC7 intracellularly (see below).

The time course of passive activation of currents carried by LTRPC7 is most consistent with activation due to diffusional depletion of a small intracellular constituent that suppresses channel opening. On the basis of the results above and the presence of the α-kinase domain in LTRPC7, we suspected that $[Mg^{2+}]_i$ and $[ATP]_i$ might be involved in LTRPC7 regulation. We therefore systematically changed the $[Mg^{2+}]_i$ and $[ATP]_i$ of our patch pipette solutions. LTRPC7 channel activity is strongly suppressed by Mg·ATP concentrations in the millimolar range (Fig. 4a, d), with nearly complete suppression of currents at 6 mM Mg·ATP. Under these conditions, free $[Mg^{2+}]_i$ varies from 670 to 800 μM, and the available ATP is essentially all in the physiological Mg·ATP form. However, no suppressive effect is observed when 2 mM Na·ATP is added to a $[Mg^{2+}]_i$-free internal solution, weighing against a role for a standard high-energy phosphate group transfer in the suppression phenomenon as well as indicating that $[Mg^{2+}]_i$ is a required factor or cofactor for inhibition. Figure 4b summarizes the average currents observed during intracellular perfusion of cells with solutions devoid of ATP but containing different free Mg^{2+} concentrations. From this, it is evident that high $[Mg^{2+}]_i$ strongly suppresses LTRPC7-dependent currents even in the absence of ATP, with 3 mM causing a complete block (Fig. 4e).

To evaluate further the potential role of high-energy phosphate transfer in suppression, we perfused cells with four different Mg^{2+}-nucleotide trisphosphates (NTP) to define the nucleotide specificity (Fig. 4c). At 2 mM (free $[Mg^{2+}]_i \approx 700–850$ μM), both ATP and GTP largely suppressed activation of LTRPC7 currents (with essentially identical dose–response curves), whereas CTP and ITP were less effective compared with NTP-free controls. If the dose–

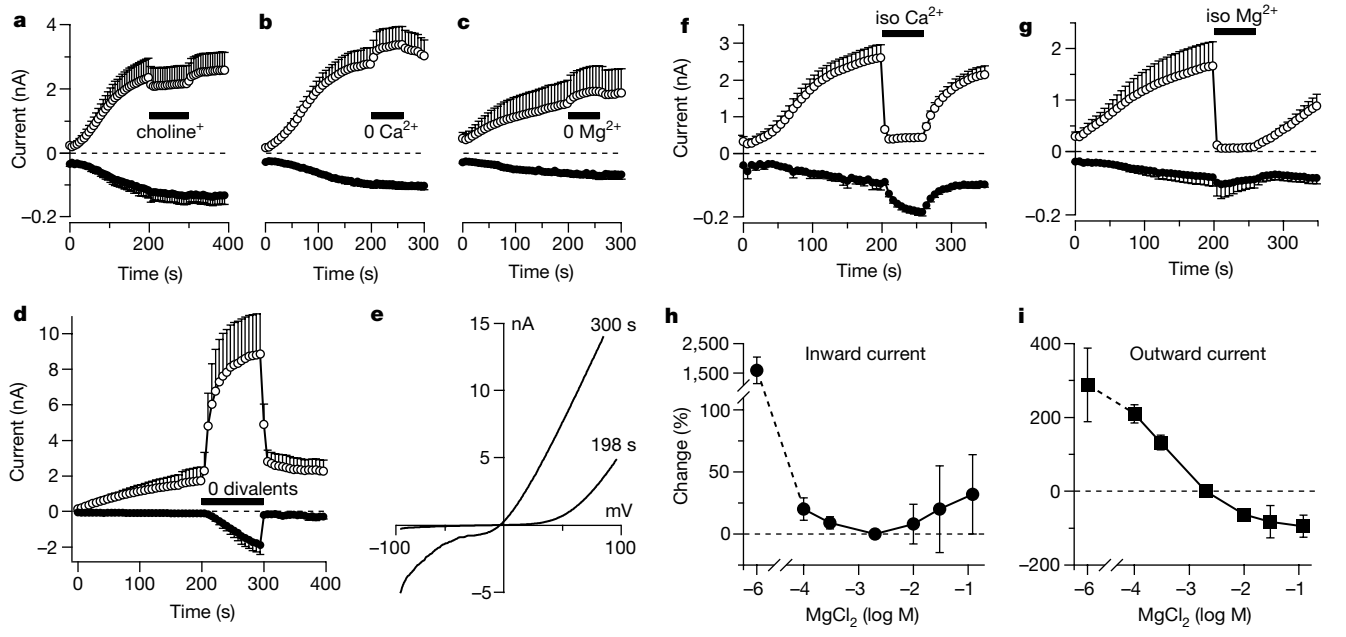

Figure 3 Permeation and block of LTRPC7 by divalent ions. Average inward and outward currents carried by recombinant LTRPC7 at –80 and +80 mV, respectively. Black bars indicate solution changes. **a**, Extracellular solutions contained 10 mM Ca^{2+} and 2 mM Mg^{2+}. Inward currents remained unaffected by application of extracellular solution in which NaCl was replaced by choline-Cl ($n = 5$). **b**, Application of Ca^{2+}-free extracellular solution ($n = 5$). **c**, Application of Mg^{2+}-free extracellular solution ($n = 5$). **d**, Removal of both Ca^{2+} and Mg^{2+} ($n = 5$). **e**, *I–V* relationship of currents under conditions as in **d** elicited before divalent-free application (198 s) and just before re-admission of divalents (300 s). **f**, **g**, Application of isotonic $CaCl_2$ or $MgCl_2$ (120 mM) reversibly enhanced inward currents and strongly inhibited outward currents ($n = 5$ each). **h**, Anomalous mole fraction behaviour of Mg^{2+} permeation. Changes in inward current measured at –80 mV as a function of extracellular Mg^{2+} concentration ($n = 3–5$; Mg^{2+}-free solution plotted at 1 μM) and normalized in reference to 2 mM extracellular Mg^{2+} (extracellular solutions were nominally Ca^{2+}-free). **i**, Analysis of the corresponding changes in outward currents (measured at +80 mV) in the same cells as in **g** (also in reference to 2 mM Mg^{2+}).

response curve for ATP (Fig. 4d) is instead plotted as a function of calculated free $[Mg^{2+}]_i$ (Fig. 4e, open boxes), it can be seen that suppression of LTRPC7 currents by Mg·ATP occurs within a range of free $[Mg^{2+}]_i$ that produces only moderate suppressive effects on LTRPC7 in the absence of ATP or GTP (Fig. 4e, filled circles). Together, these results would be most consistent with Mg·ATP acting as a physiological regulator of LTRPC7, as cellular levels of free $[Mg^{2+}]_i$ are around 0.5 mM (ref. 3) and cytosolic GTP levels are at least five times lower than those of ATP, which are typically several millimolar[4].

Finally, as a further test of a role for a high-energy phosphate transfer reaction in LTRPC7 gating, we performed experiments with Na·ATP-γ-S and Mg·ATP-γ-S, non-hydrolysable analogues of ATP. Because ATP-γ-S can be used by protein kinases in thio-phosphorylation reactions, and thio-phosphate linkages are not susceptible to protein phosphatases, the result is irreversible protein phosphorylation. As shown in Fig. 4f (open diamonds), 2 mM Mg·ATP-γ-S (free $[Mg^{2+}]_i \approx 700\ \mu M$) effectively suppresses LTRPC7 currents. To address the question of whether this suppression is due to irreversible thio-phosphorylation of LTRPC7, we performed experiments in which cells were initially patched with pipette solutions containing Mg·ATP-γ-S (filled circles in Fig. 4f) and subsequently re-patched around 180 s later, this time with an ATP-free pipette solution to wash out Mg·ATP-γ-S. This resulted in essentially full re-development of LTRPC7 currents, demonstrating the reversibility of the suppression phenomenon under conditions in which the participation of a phosphorylation event should have resulted in irreversible suppression. Therefore, the suppression of LTRPC7 activation by Mg·ATP-γ-S is analogous to that of Mg·ATP or Mg·GTP and is likely to be the result of direct regulation of channel activity. By the same logic, Na·ATP-γ-S should behave similarly to Na·ATP and this is confirmed in Fig. 4f (open circles), where 2 mM Na·ATP-γ-S failed to suppress LTRPC7 activation. We did observe a Na·ATP-γ-S-mediated delayed and slow inactivation, which may involve phosphorylation events that downregulate LTRPC7 activity.

We also analysed endogenous currents activated in several cultured cell lines from tissues positive for LTRPC7 transcripts, using the same experimental conditions that produced maximal LTRPC7 activation in our heterologous HEK-293 system. Each cell type analysed (Fig. 5) possessed currents with Mg·ATP sensitivity and current–voltage relationship similar to those observed in HEK-293 cells overexpressing LTRPC7. In particular, the native currents exhibited strong outward rectification at potentials above +50 mV, which may be considered the signature of this conductance. We have adopted the convention that native currents that exhibit sensitivity to Mg·nucleotide complexes and permeation properties like those of LTRPC7 are designated as magnesium·nucleotide-regulated metal ion currents or MagNuM. Our data indicate that LTRPC7 mediates most or all of MagNuM in all cell types so far analysed.

An analysis of LTRPC7 function has also been performed by Clapham and colleagues[5]. They concluded that the EEF2α domain kinase activity was required for channel gating. However, this conclusion was based in part on increased currents observed upon addition of 5 mM Na·ATP to a standard intracellular solution containing only 1 mM $MgCl_2$, reducing free $[Mg^{2+}]_i$ to 6 μM. As our data show Mg^{2+} to be an essential (co)factor in regulating LTRPC7 activity, such a drop in free $[Mg^{2+}]_i$ would be expected to produce a large relative increase in current amplitude independent of ATP, suggesting that conclusions regarding the role of the kinase domain in channel activation should be taken cautiously. Clapham and

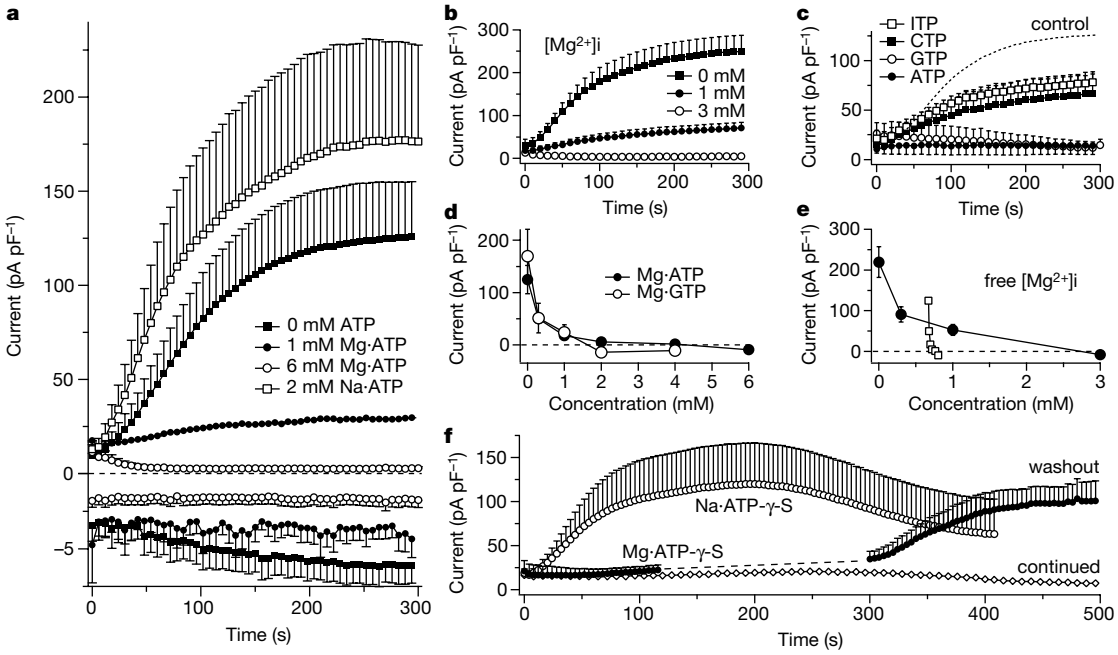

Figure 4 LTRPC7 gating is modulated by $[Mg^{2+}]_i$ and Mg·nucleotides. **a**, Average inward and/or outward currents carried by recombinant LTRPC7 at –80 and +80 mV, respectively. Cells were perfused with internal solutions containing various ATP concentrations (0 mM Mg·ATP, $n = 7$; 1 mM Mg·ATP, $n = 5$; 6 mM Mg·ATP, $n = 5$; 2 mM Na·ATP, $n = 5$). **b**, Cells were perfused with internal solutions containing the indicated $MgCl_2$ concentrations in the absence of added ATP (in all cases $n = 5$). **c**, Cells were perfused with internal solutions containing 2 mM of various Mg·nucleotides (in all cases $n = 5$). Dotted control trace represents 0 ATP taken from **a**. **d**, Average changes of maximum outward current measured at +80 mV as a function of intra-pipette Mg·ATP or Mg·GTP levels. The change in current size was analysed by subtracting the first data trace acquired after whole-cell establishment from the one elicited at 300 s. **e**, Average changes of maximum outward current measured at +80 mV as a function of intra-pipette free Mg^{2+} levels in the absence of added ATP (filled circles). The change in current size was analysed as in **d**. Open squares, data points of the ATP dose–response curve in **d**, here plotted against the calculated free Mg^{2+} under those conditions. **f**, Cells were perfused with internal solutions containing 2 mM of various non-hydrolysable analogues of ATP (Na·ATP-γ-S, open circles, $n = 6$; Mg·ATP-γ-S, open diamonds, $n = 3$). Filled circles represent three cells perfused with 2 mM Mg·ATP-γ-S for 120 s and then re-patched with ATP-free solution. Data sets from re-patched cells were aligned, averaged and plotted with a delay of 180 s, which represents the average time needed to exchange pipettes and re-patch individual cells (120 s, 198 s, 215 s, respectively).

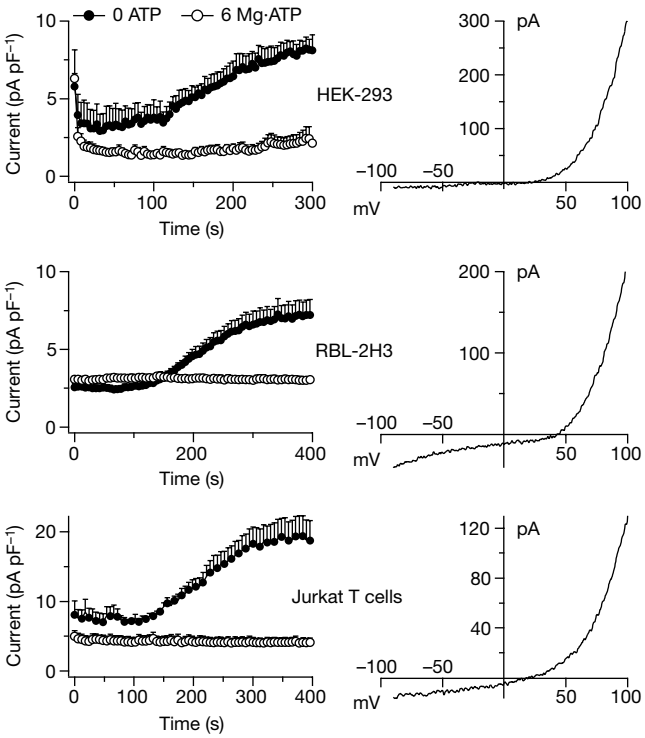

Figure 5 Mg·ATP sensitive conductances with LTRPC7 signature are ubiquitous. Wild-type HEK-293, RBL-2H3 and Jurkat T-lymphocytes were perfused with standard internal solutions supplemented with either 6 mM ATP (open circles; $n = 5$, ± s.e.m.) or no ATP (filled circles; $n = 5$, ± s.e.m.). Under these experimental conditions the store-operated Ca^{2+} current I_{CRAC} contributes a larger proportion of inward currents than when LTRPC7 is overexpressed, accounting for the right-shift in reversal potential.

colleagues also concluded, on the basis of reversal potential measurements, that LTRPC7 is essentially non-selective for monovalent relative to divalent cations. However, as monovalent and divalent ions do not permeate LTRPC7 independently (Fig. 3), the permeation of LTRPC7 at physiological membrane potentials (−40 to −80 mV) is selective for divalent ions, whereas monovalent permeation becomes significant only at rather positive potentials.

In conclusion, we have cloned a member of the LTRPC family of ion channels, designated LTRPC7, and analysed its role in cellular function. Our data indicate that LTRPC7 is an intracellular ligand-gated ion channel whose activation may be linked to cellular energy metabolism through its sensitivity to cytosolic Mg·ATP levels, and that it effectively permeates both Ca^{2+} and Mg^{2+}. As loss of LTRPC7 function would presumably disrupt the coordination of cellular energy production with the homeostasis of these (and possibly other) divalent cations, these functional characteristics plausibly account for the cellular death that occurs in standard cell culture conditions upon deletion of the DT-40 LTRPC7 genes. Furthermore, because of its link to cellular energy metabolism, LTRPC7 may represent a direct mediator of the toxic divalent cation entry that occurs during severe metabolic stress conditions such as hypoxia or hypoglycaemia. □

Methods

Expression analysis

RT–PCR (PCR with reverse transcription) analysis was performed from the indicated human tissue complementary DNA libraries according to the manufacturer's protocols (Life Technologies). For LTRPC7, oligonucleotides used were GTCACTTGGAAACTGG AACC and CGGTAGATGGCCTTCTACTG to produce a 278-base-pair (bp) band. PCR was performed using standard techniques and 30 cycles of 94 °C for 30 s, 55 °C for 30 s, and 72 °C for 60 s. The approximate intensity of the ethidium bromide staining of correct sized bands was estimated by eye to be 1–2+. The LTRPC7 primers used in these reactions were generated from initial expressed sequence tag sequences, and contain a single base pair mismatch at the 5′ end of the primer based on the corresponding region of LTRPC7 sequence obtained from subsequent clones. Multiple tissue northern blots for human tissues and cell lines were obtained from Clontech and all hybridizations were performed according to the manufacturer's protocols. LTRPC7 northern blots were performed using a dUTP-labelled RNA probe generated from a 500-bp fragment corresponding to approximately residues 1,695–2,195 of the human LTRPC7 transcript. The probe was generated using a T7-directed RNA probe synthesis kit from Ambion.

Electrophysiology

HEK-293 cells transfected with the Flag–murineLTRPC7/pCDNA4-TO construct were grown on glass coverslips with DMEM supplemented with 10% fetal bovine serum, blasticidin (5 μg ml^{-1}), and zeocin (0.4 mg ml^{-1}). LTRPC7 expression was induced by adding 1 μg ml^{-1} tetracycline to the culture medium. Whole-cell patch-clamp experiments were performed at 21–25 °C 18–24 h after induction, using cells grown on glass coverslips and kept in a standard modified Ringer's solution of the following composition (in mM): NaCl 145, KCl 2.8, CsCl 10, $CaCl_2$ 1, $MgCl_2$ 2, glucose 10, HEPES·NaOH 10, pH 7.2. In some experiments, nominally $Ca^{2+}$and/or Mg^{2+}-free extracellular solutions or isotonic $CaCl_2$ and $MgCl_2$ solutions (120 mM) were applied by pressure ejection from wide-tipped pipettes. Intracellular pipette-filling solutions contained (in mM): Cs-glutamate 145, NaCl 8, $MgCl_2$ 1, Cs-BAPTA 10, HEPES·CsOH 10, pH 7.2. In some experiments, Cs-glutamate was replaced equimolarly by K-glutamate or choline-chloride. Free [Mg^{2+}]i was calculated by Patcher's Power Tools (http://www.wavemetrics.com/Users/ppt.html). High-resolution current recordings were acquired by a computer-based patch-clamp amplifier system (EPC-9, HEKA). Immediately following establishment of the whole-cell configuration, voltage ramps of 50-ms duration spanning the voltage range of −100 to +100 mV were delivered from a holding potential of 0 mV at a rate of 0.5 Hz over a period of 200–400 s. All voltages were corrected for a liquid junction potential of 10 mV between external and internal solutions when internal solutions contained glutamate. Currents were filtered at 2.3 kHz and digitized at 100-μs intervals. Capacitive currents and series resistance were determined and corrected before each voltage ramp using the automatic capacitance compensation of the EPC-9. The low-resolution temporal development of currents at a given potential was extracted from individual ramp current records by measuring the current amplitudes at voltages of −80 mV or +80 mV.

Full methods for all cloning, construction of expression constructs, SDS–PAGE and immunoprecipitation analyses, and construction of DT-40 cell lines are available as Supplementary Information.

Received 5 December 2000; accepted 23 April 2001.

1. Harteneck, C., Plant, T. D. & Schultz, G. From worm to man: three subfamilies of TRP channels. *Trends Neurosci.* **23,** 159–166 (2000).
2. Ryazanov, A. G. *et al.* Identification of a new class of protein kinases represented by eukaryotic elongation factor-2 kinase. *Proc. Natl Acad. Sci. USA* **94,** 4884–4889 (1997).
3. Romani, A. M. & Scarpa, A. Regulation of cellular magnesium. *Front. Biosci.* **5,** D720–734 (2000).
4. Luthi, D., Gunzel, D. & McGuigan, J. A. Mg-ATP binding: its modification by spermine, the relevance to cytosolic Mg^{2+} buffering, changes in the intracellular ionized Mg^{2+} concentration and the estimation of Mg^{2+} by ^{31}P-NMR. *Exp. Physiol.* **84,** 231–252 (1999).

5. Runnels, L. W., Yue, L. & Clapham, D. E. TRP-PLIK, a bifunctional protein with kinase and ion channel activities. *Science* **291,** 1043–1047 (2001).

Supplementary Information is available at *Nature*'s World-Wide Web site (http://www.nature.com) or as paper copy from the London editorial office of *Nature*.

Acknowledgements

We thank D. Tani and M. Monteilh-Zoller for technical assistance. This work was funded in part by a Beth Israel Pathology Foundation grant and a BIDMC Fireman Fellowship award to A.M.S., and a NIH grant. A.-L.P. is supported by the German Academic Exchange Service (DAAD).

Correspondence and requests for materials should be addressed to A.M.S. (e-mail: andrewms@u.washington.edu). The GenBank accession numbers for murine and human LTRPC7 cDNA and protein sequences are AY032951 and AY032950, respectively.

ADP-ribose gating of the calcium-permeable LTRPC2 channel revealed by Nudix motif homology

Anne-Laure Perraud*†, Andrea Fleig†‡, Christopher A. Dunn†§, Leigh Ann Bagley‡, Pierre Launay*, Carsten Schmitz*, Alexander J. Stokes*, Qiqin Zhu*, Maurice J. Bessman§, Reinhold Penner‡, Jean-Pierre Kinet* & Andrew M. Scharenberg*‖

** Department of Pathology, Beth Israel Deaconess Medical Center and Harvard Medical School, Boston, Massachusetts 02215, USA*
‡ Laboratory of Cell and Molecular Signaling, Center for Biomedical Research at The Queen's Medical Center and John A. Burns School of Medicine at the University of Hawaii, Honolulu, Hawaii 96813, USA
§ Department of Biology, Johns Hopkins University, Baltimore, Maryland 21218, USA
† These authors contributed equally to this work.

Free ADP-ribose (ADPR), a product of NAD hydrolysis and a breakdown product of the calcium-release second messenger cyclic ADPR (cADPR), has no defined role as an intracellular signalling molecule in vertebrate systems. Here we show that a 350-amino-acid protein (designated NUDT9) and a homologous domain (NUDT9 homology domain) near the carboxy terminus of the LTRPC2/TrpC7 putative cation channel[1] both function as specific ADPR pyrophosphatases. Whole-cell and single-channel analysis of HEK-293 cells expressing LTRPC2 show that LTRPC2 functions as a calcium-permeable cation channel that is specifically gated by free ADPR. The expression of native LTRPC2 transcripts is detectable in many tissues including the U937 monocyte cell line, in which ADPR induces large cation currents (designated I_{ADPR}) that closely match those mediated by recombinant LTRPC2. These results indicate that intracellular ADPR regulates calcium entry into cells that express LTRPC2.

The LTRPC family of putative ion channel proteins[2] has a unique amino-terminal region of 600–700 amino acids that can be divided into 4 smaller sub-regions based on their high level of conservation in one or more family members. Next there is a region of around 300 amino acids that contains the putative pore-forming transmembrane spans, and then a region with predicted coiled-coil character, and finally a C-terminal extension of variable length and unique structure for individual LTRPC members. Figure 1a illustrates the structural elements of LTRPC2, which was originally designated TrpC7 (ref. 1), but was named LTRPC2 in a recently proposed nomenclature[2].

Whereas northern blotting indicates that LTRPC2 was dominantly expressed in brain (data not shown, consistent with previous reports[1]), polymerase chain reaction after reverse transcription of RNA (RT–PCR) detected LTRPC2 transcripts in many other tissues, including bone marrow, spleen, heart, leukocytes, liver and lung (data not shown). Specificity of the RT–PCR analysis was confirmed by cloning a full-length LTRPC2 transcript from a human monocyte complementary DNA library. On the basis of its unique C-terminal structure, we subsequently cloned a new cDNA from a spleen cDNA library, designated NUDT9. Its expression was detectable by RT–PCR in every tissue analysed, including bone marrow, spleen, heart, leukocytes, liver, lung, kidney, prostate, testis and skeletal muscle (data not shown). The C-terminal region of LTRPC2 and NUDT9 share 50% homology and are also homologous to the *Caenorhabditis elegans* predicted protein EEED8.8 (Fig. 1b). Sequence analysis of NUDT9 revealed the presence of a putative signal peptide/anchor and a Nudix box sequence motif. Nudix boxes are found in a family of diverse enzymes that catalyse the hydrolysis of nucleoside diphosphate derivatives[3]. This motif is highly conserved in EEED8.8, and is present in a less conserved form in the NUDT9 homology region (NUDT9-H) of LTRPC2.

On the basis of the presence of the Nudix box in NUDT9 and the homology between NUDT9 and LTRPC2, we thought that identifying a potential substrate for NUDT9 would provide insight into LTRPC2 function. We therefore expressed NUDT9 in *Escherichia coli*, purified the protein, and screened a series of nucleoside diphosphate derivatives for enzymatic activity. The recombinant protein was a highly specific ADPR pyrophosphatase (yielding AMP and ribose 5-phosphate) with a K_m of 100 ± 10 μM and a V_{max} of 11.8 ± 0.3 μmol min^{-1} mg^{-1} protein. We then expressed the LTRPC2. NUDT9-H in *E. coli* and evaluated its activity towards the same panel of substrates. NUDT9-H had the same specific ADPR pyrophosphatase activity and an identical K_m (100± 10 μM), but a far lower level of activity (V_{max} = 0.1 μmol min^{-1} mg^{-1}). This may be because of the substitution of RIL and QE amino acids in LTRPC2 for the conserved REF triad and EE diad found in the Nudix motifs of NUDT9 and EEED8.8, as these are important for the catalytic activity of other Nudix hydrolases[3]. However, we cannot exclude that the reduced activity of the LTRPC2 NUDT9-H domain relative to that of NUDT9 may be because it is not in its native protein context.

The simplest model to relate NUDT9/NUDT9-H activity to LTRPC2 function is to have LTRPC2 as an ion channel somehow regulated by ADPR. To test this, we used a human embryonic kidney cell line (HEK-293) with tetracycline-regulated transcription of a Flag-tagged LTRPC2 construct. As can be seen in Fig. 2a, in wild-type cells, no transcript was detectable using an LTRPC2-specific probe. After tetracycline induction of cells stably transfected with a textracycline-controlled LTRPC2 construct, substantial expression of an around 6-kilobase (kb) recombinant LTRPC2 transcript was detectable. Similarly, anti-Flag immunoreactive protein of the correct predicted molecular mass was detected in western blots only after tetracycline induction of the stably transfected cells (Fig. 2b). Finally, anti-Flag immunofluorescence indicated that a significant portion of LTRPC2 was localized at or near the plasma membrane (Fig. 2c); this led us to perform patch-clamp analyses of plasma-membrane currents. Without tetracycline induction, ADPR has no detectable effect on plasma-membrane currents (Fig. 2d). Furthermore, in the absence of ADPR in the patch pipette, basal currents in tetracycline-treated cells are the same as in wild-type HEK-293 cells. This indicates that LTRPC2 is not open constitutively under our conditions of standard intracellular solutions. In contrast, after tetracycline induction, large inward and outward currents reversing at 0 mV were induced by 100 μM ADPR (Fig. 2d; Fig. 2e, linear *I–V* curves at various times of current development). No current activation was observed using 100 μM of a variety of closely related molecules, including NAD^+, cADPR, ATP, ADP,

‖ Present address: Department of Pediatrics and Immunology, University of Washington and Children's Hospital and Medical Center, Seattle, Washington 98195-6320, USA.

experiment advances the close analogy between the macroscopic quantum physics of superconductivity and superfluidity. Both systems exhibit persistent currents, quantized circulation (fluid and magnetic), sinϕ weak links and now, double-path quantum interference. □

Methods

To derive equation (2) we follow a heuristic method similar to that which Feynman[24] applied to the analogous superconducting case. Consider the interferometer in Fig. 1a to be rotating at angular velocity Ω. The total external current passing through the interferometer may be written as:

$$I_t = I_c \sin\phi_1 + I_c \sin\phi_2 = 2I_c \cos\left(\frac{\phi_1 - \phi_2}{2}\right)\sin\left(\frac{\phi_1 + \phi_2}{2}\right) \quad (5)$$

We assume that the fluid in the torus is characterized at every point by a quantum phase factor which is macroscopically coherent. The rotation of the torus entrains the superflow which is then almost that of a solid body, $v_s = \Omega R$. Around a closed path in the interferometer, as indicated by the dotted line in Fig. 1, the phase can change only in multiples of 2π.

$$\oint \nabla\phi \cdot d\mathbf{l} = 2\pi n = \int_a^b \frac{2m_3}{\hbar} \mathbf{v}_s \cdot d\mathbf{l} + \phi_1 + \int_c^d \frac{2m_3}{\hbar} \mathbf{v}_s \cdot d\mathbf{l} - \phi_2 = -\frac{2m_3}{\hbar} 2\Omega\pi R^2 + \phi_1 - \phi_2 \quad (6)$$

The limit points, a–d, in the integrals are shown in Fig. 1a. In equation (6) we have used the concept[25] that the phase gradient is proportional to superfluid velocity, $\nabla\phi = (2m_3\mathbf{v}_s)/\hbar$. Equation (6) may be solved for $\phi_1 - \phi_2$, which, when inserted into equation (5) gives

$$I_t = I_c^* \sin\Phi \quad (7)$$

where $\Phi \equiv (\phi_1 + \phi_2)/2$ is the phase difference across the ends of the interferometer. We see that the rotating interferometer behaves as a single Josephson weak link, whose maximum current is given by the quantum interference term:

$$I_c^* = 2I_c \left|\cos\left(\pi \frac{2\Omega \cdot \mathbf{A}}{\kappa_3}\right)\right| \quad (8)$$

Here $\kappa_3 \equiv \hbar/(2m_3)$ is the quantum of circulation, **A** is the interferometer area vector, normal to the plane, and we have included a scalar product describing the more general case when the rotation axis is not parallel to **A**.

Received 5 March; accepted 14 May 2001.

1. Young, T. *A Course of Lectures in Natural Philosophy and the Mechanical Arts* Vol. 1, 364 (London, 1845); also as facsimile edition (New York, 1971).
2. Davisson, C. J. Are Electrons Waves? *Franklin Inst. J.* **205,** 597 (1928).
3. Werner, S. A., Studenmann, J. L. & Colella, R. Effect of Earth's rotation on the quantum mechanical phase of the neutron. *Phys. Rev. Lett.* **42,** 1103–1106 (1979).
4. Keith, D. W., Ekstrom, C. R., Turchette, Q. A. & Pritchard, D. E. An interferometer for atoms. *Phys. Rev. Lett.* **66,** 2693–2696 (1991).
5. Andrews, M. R. *et al.* Observation of interference between two Bose condensates. *Science* **275,** 637–641 (1997).
6. Barone, A. & Paterno, G. *Physics and Application of the Josephson Effect* (Wiley, New York, 1982).
7. Varoquaux, E. & Avenel, O. Josephson effect and quantum phase slippage in superfluids. *Phys. Rev. Lett.* **60,** 416–419 (1988).
8. Pereversev, S. V., Loshak, A., Backhaus, S., Davis, J. C. & Packard, R. E. Quantum oscillations between two weakly coupled reservoirs of superfluid ^{3}He. *Nature* **388,** 449–451 (1997).
9. Marchenkov, A. *et al.* Bi-state superfluid ^{3}He weak links and the stability of Josephson π states. *Phys. Rev. Lett.* **83,** 3860–3863 (1999).
10. Packard, R. E. & Vitale, S. Principle of superfluid-helium gyroscopes. *Phys. Rev. B* **46,** 3540–3549 (1992).
11. Gustavson, T. L., Bouyer, P. & Kasevitch, M. A. Physical rotation measurements with an atom interferometer gyroscope. *Phys. Rev. Lett.* **78,** 2046–2049 (1997).
12. Stedman, G. E. Ring-laser tests of fundamental physics and geophysics. *Rep. Prog. Phys.* **60,** 615–687 (1997).
13. Anderson, P. W. in *Progress in Low Temperature Physics* (ed. Gorter, C. J.) 1–44 (North Holland, Amsterdam, 1967).
14. Marchenkov, A., Simmonds, R. W., Davis, J. C. & Packard, R. E. Observation of the Josephson plasma mode for a superfluid ^{3}He weak link. *Phys. Rev. B* **61,** 4196–4199 (2000).
15. Schwab, K., Bruckner, N. & Packard, R. E. Detection of the Earth's rotations using superfluid phase coherence. *Nature* **386,** 585–587 (1997).
16. Avenel, O., Hakonen, P. & Varoquaux, E. Detection of the rotation of the Earth with a superfluid gyrometer. *Phys. Rev. Lett.* **78,** 3602–3605 (1997).
17. Mukharsky, Yu., Varoquaux, E. & Avenel, O. Current-phase relationship measurements in the flow of superfluid ^{3}He through a single orifice. *Physica B* **280,** 130–131 (2000).
18. Mukharsky, Yu., Avenel, O. & Varoquaux, E. Rotation measurements with a superfluid ^{3}He gyrometer. *Physica B* **284–288,** 287–288 (2000).
19. Rowe, C. H. *et al.* Design and operation of a very large ring laser gyroscope. *Appl. Opt.* **38,** 2516–2523 (1999).
20. Gustavson, T. L., Landragin, A. & Kasevich, M. A. Rotation sensing with a dual atom interferometer Sagnac gyroscope. *Class. Quant. Gravity* **17,** 2385–2398 (2000).
21. Herring, T. A. The rotation of the Earth. *Rev. Geophys. Suppl.* **29,** 172–175 (1991).
22. Clarke, J. in *SQUID Sensors: Fundamentals, Fabrication and Applications* (ed. Weinstock, H.) (Kluwer Academic, 1996).
23. Simmonds, R. W., Marchnkov, A., Vitale, S., Davis, J. C. & Packard, R. E. New flow dissipation mechanisms in superfluid ^{3}He. *Phys. Rev. Lett.* **84,** 6062–6065 (2000).
24. Feynmann, R. P., Leighton, R. B. & Sands, M. *The Feynman Lectures in Physics* Vol. 3, Ch. 21 (Addison Wesley, Reading, Massachusetts, 1963).
25. Tilley, D. R. & Tilley, J. *Superfluidity and Superconductivity* 3rd edn 171 (Hilger, Bristol, 1990).
26. Paik, H. J. Superconducting tunable-diaphragm transducer for sensitive acceleration measurements. *J. Appl. Phys.* **47,** 1168–1178 (1976).

Acknowledgements

We thank S. Vitale and K. Penanen for discussions; Y. Sato for assistance; A. Loshak for making the aperture arrays; and E. Crump, D. Mathews and C. Ku for assistance in improving noise conditions in our building. This work was supported in part by NASA, the Office of Naval Research, the National Science Foundation, and the Miller Institute for Basic Research (J.C.D.).

Correspondence and requests for materials should be addressed to R.P. (e-mail: packard@socrates.berkeley.edu).

Coexistence of superconductivity and ferromagnetism in the *d*-band metal $ZrZn_2$

C. Pfleiderer*, M. Uhlarz*, S. M. Hayden†, R. Vollmer*, H. v. Löhneysen*‡, N. R. Bernhoeft§ & G. G. Lonzarich‖

* *Physikalisches Institut, Universität Karlsruhe, D-76128 Karlsruhe, Germany*
† *H. H. Wills Physics Laboratory, University of Bristol, Bristol BS8 1TL, UK*
‡ *Forschungszentrum Karlsruhe, Institut für Festkörperphysik, D-76021 Karlsruhe, Germany*
§ *DRFMC-SPSMS, CEA Grenoble, F-38054 Grenoble, Cedex 9, France*
‖ *Cavendish Laboratory, University of Cambridge, Madingley Road, Cambridge CB3 0HE, UK*

It has generally been believed that, within the context of the Bardeen–Cooper–Schrieffer (BCS) theory of superconductivity, the conduction electrons in a metal cannot be both ferromagnetically ordered and superconducting[1,2]. Even when the superconductivity has been interpreted as arising from magnetic mediation of the paired electrons, it was thought that the superconducting state occurs in the paramagnetic phase[3,4]. Here we report the observation of superconductivity in the ferromagnetically ordered phase of the *d*-electron compound $ZrZn_2$. The specific heat anomaly associated with the superconducting transition in this material appears to be absent, and the superconducting state is very sensitive to defects, occurring only in very pure samples. Under hydrostatic pressure superconductivity and ferromagnetism disappear at the same pressure, so the ferromagnetic state appears to be a prerequisite for superconductivity. When combined with the recent observation of superconductivity in UGe_2 (ref. 4), our results suggest that metallic ferromagnets may universally become superconducting when the magnetization is small.

The compound $ZrZn_2$ was first investigated by Matthias and Bozorth[5] in the 1950s, who discovered that it was ferromagnetic despite being made from nonmagnetic, superconducting constituents. $ZrZn_2$ crystallizes in the C15 cubic Laves structure, as shown in the inset of Fig. 1, with lattice constant $a = 7.393$ Å. The Zr atoms form a tetrahedrally coordinated diamond structure and the magnetic properties of the compound derive from the Zr 4*d* orbitals, which have a significant direct overlap[6]. Ferromagnetism develops

below the Curie temperature $T_{FM} = 28.5$ K with a small ordered moment $\mu_s = 0.17\mu_B$ per formula unit. $ZrZn_2$ has a large electronic heat capacity at low temperatures $C/T = 47$ mJ K^{-2} mol^{-1} signalling an abundance of low-energy magnetic excitations in addition to conventional spin-wave contributions[7]. The low Curie temperature and small ordered moment render $ZrZn_2$ special among stoichiometric ferromagnetic metals and indicate that the compound is close to a ferromagnetic quantum critical point. The most remarkable magnetic property of $ZrZn_2$ is the effect of a magnetic field on the ordered moment[5]. Figure 1 shows the magnetization of $ZrZn_2$ as a function of magnetic field. At $T = 1.75$ K a relatively small field $\mu_0 H = 0.05$ T is required to form a single ferromagnetic domain. On further increasing the field, the ordered moment is rapidly increased with a field of 6 T causing a 50% increase in the ordered moment, which is unsaturated up to 35 T, the highest field measured[8]. This behaviour contrasts strongly with the elemental ferromagnets Fe, Ni and Co, in which, after a single domain is formed, fields applied parallel to the easy axis have only a small effect on the ordered moment.

The proximity of $ZrZn_2$ to a ferromagnetic quantum critical point has led to numerous proposals that it might be a superconductor[9–11]. We have therefore studied the resistivity, a.c. (differential) susceptibility and specific heat capacity of high-purity $ZrZn_2$ at low temperatures. Figure 2 shows measurements of the basic physical properties of $ZrZn_2$ for two samples of differing quality. The highest-quality sample (C) has a low-temperature residual resistivity of 0.62 μΩ cm consistent with charge carrier mean free paths of several hundred ångströms. Figure 2a shows that there is a rapid drop in the electrical resistivity below a temperature of $T_{SC} = 0.29$ K, suggesting a transition to superconductivity. The resistance drop is absent in the lower-quality sample (sample A), which has a residual impurity scattering rate five times higher than sample C. The application of a field of 0.2 T suppresses the drop, as expected for a superconducting transition. A second signature of superconductivity is the diamagnetic screening of a magnetic field, which can be observed in the a.c. susceptibility. Because $ZrZn_2$ is

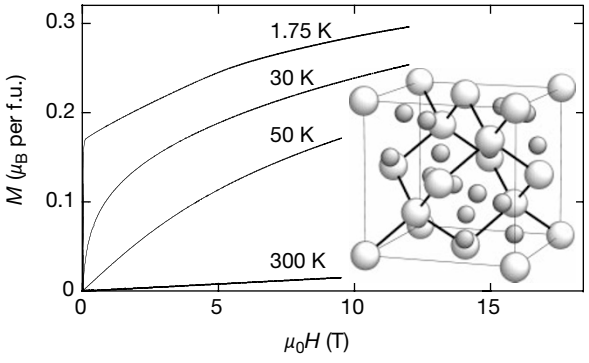

Figure 1 Magnetization curves and crystal structure of $ZrZn_2$. A spontaneous moment μ_s develops below the Curie temperature $T_{FM} = 28.5$ K. For $T = 1.75$ K, we find a spontaneous moment $\mu_s = 0.17\mu_B$ per formula unit (f.u.) and a coercive field (determined from a hysteresis loop) of $\mu_0 H^* = 2 \times 10^{-3}$ T (μ_B: Bohr magneton). The increase of the ordered moment with field demonstrates the unsaturated nature of the ordered moment and indicates the presence of a large longitudinal susceptibility. Inset, the cubic C15 Laves phase unit cell of $ZrZn_2$, where the Zr atoms (large spheres) form a tetrahedrally coordinated diamond structure. The samples investigated here were grown by a directional-cooling method[23] in which zone-refined Zr and Zn were melted in a high-purity Y_2O_3 crucible sealed inside a Ta pressure container. Single crystals were cut from the resulting ingot by spark erosion. Neutron and Laue X-ray diffraction spectra were consistent with the C15 structure previously reported. Electron-probe microanalysis revealed no impurity phases or segregations of the constituent elements at the resolution limit of 0.5%.

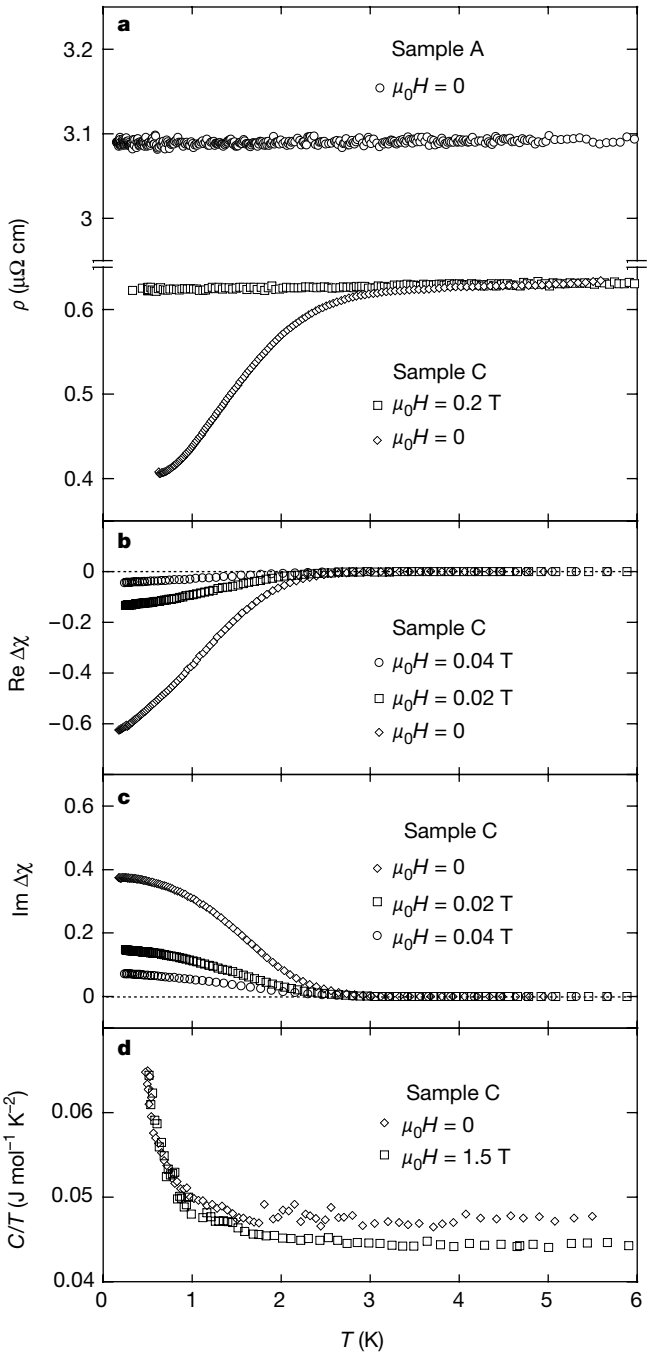

Figure 2 Evidence of superconductivity in high-purity single crystals of weakly ferromagnetic $ZrZn_2$. **a**, Resistivity versus temperature, $\rho(T)$, at $\mu_0 H = 0$ and 0.2 T, respectively, as measured in a dilution refrigerator using a four-terminal a.c. technique. Sample A (non-superconducting) is of lower quality than sample C, that is, sample A has a five times higher residual resistivity ρ_0. **b**, Real (reactive) part of the low-amplitude a.c. susceptibility in SI units versus temperature for an a.c. amplitude of 10^{-6} T, Re$\Delta\chi(T)$, at various superposed d.c. fields after subtraction of the background due to the ferromagnetism. Measurements were performed at low frequencies with a miniature susceptometer comprised of a primary and a balanced pair of secondary coils. The background was extrapolated from the T-independent susceptibility above T_{SC}, the superconducting ordering temperature. For the lowest excitation amplitudes Re$\Delta\chi(T)$ approaches almost complete diamagnetic shielding: −0.65 (near −1). An analogous diamagnetic contribution is absent in the low-quality sample (sample A) (not shown). **c**, Imaginary (dissipative) part of the a.c. susceptibility, Im$\Delta\chi(T)$. Below T_{SC} a substantial contribution develops, typical of type II superconductors. **d**, Specific heat divided by temperature versus temperature, $C/T(T)$, at $\mu_0 H = 0$ and 1.5 T as measured in a dilution refrigerator by a conventional heat pulse relaxation technique. The field-independent upturn below 0.15 K is related to nuclear quadrupolar contributions of Zr.

ferromagnetic, the a.c. susceptibility, $\chi = dM/dH$, has a large component that is due to ferromagnetic domain alignment at low fields. We have therefore subtracted a temperature-independent background, measured above T_{SC}, from our susceptibility data. Figure 2 shows the resulting real (reactive) and imaginary (dissipative) parts of the susceptibility, $Re\Delta\chi$ and $Im\Delta\chi$ respectively. A strong diamagnetic signal in $Re\Delta\chi$ associated with superconducting screening is observed below $T_{SC} = 0.29$ K. For the lowest excitation amplitudes $Re\Delta\chi$ approaches −0.65 as $T \rightarrow 0$, comparable with the ideal value of −1. A concomitant increase in the dissipative component $Im\Delta\chi$ is observed, as for other type II superconductors. The a.c. susceptibility of the low-quality sample (sample A) does not exhibit any signs of a diamagnetic contribution. We have also performed SQUID (superconducting quantum interference device) d.c. magnetization measurements below 1 K on sample C (not shown). The zero-field-cooled d.c. magnetization corresponds quantitatively with $Re\Delta\chi$, as expected, while the field-cooled magnetization shows a negligible Meissner effect (flux expulsion), as do oxide superconductors. The low-temperature specific heat is shown in Fig. 2d. In the temperature range around T_{SC} no anomaly is observed, and the normal-state electronic contribution of $C/T = 47\ mJ\ mol^{-1}\ K^{-2}$ prevails. The specific heat shows a pronounced increase below 0.15 K, which is unaffected by the application of a 1.5-T magnetic field, suggesting that it is not associated with the superconductivity, but rather with a nuclear quadrupolar contribution.

The field dependence of the a.c. susceptibility allows us to identify the critical field $\mu_0 H_{c2}$ below which superconductivity appears. A typical trace showing the rapid increase of $Im\chi$ as the field is lowered through $\mu_0 H_{c2}$ is shown in the inset of Fig. 3. From the temperature dependence of this onset field we have determined the superconducting phase diagram shown in Fig. 3. At the lowest temperatures investigated, $T = 25$ mK, we find $\mu_0 H_{c2} = 0.4$ T, which corresponds to a superconducting coherence length of $\xi = 290$ Å.

It has been known for some time that the ferromagnetism in $ZrZn_2$ is rapidly suppressed under pressure[12]. This, and the prediction that superconductivity is controlled by the quantum critical point where ferromagnetism disappears at zero temperature, led us to perform high-pressure studies. Figure 4 summarizes the effect of pressure on the Curie temperature, T_{FM}, and the superconducting-transition temperature, T_{SC}. Hydrostatic pressure suppresses both the ferromagnetism and the superconductivity above a critical pressure of $P_c = 21$ kbar. Thus, it is not sufficient to be close to the ferromagnetic quantum critical point for superconductivity to occur in $ZrZn_2$; the compound must also be in the ferromagnetic state.

The superconductivity in $ZrZn_2$ has a number of remarkable features. First, it only appears to occur in high-purity single-crystal samples. Unconventional or non-*s*-wave forms of superconductivity generally require the superconducting coherence length $\xi = 290$ Å to be somewhat smaller than the electronic mean free path l_0 (ref. 13). Thus, in view of its sensitivity in $ZrZn_2$ to the quality of the sample, the superconductivity in $ZrZn_2$ is likely to be unconventional. Second, there is no superconducting anomaly in the specific heat. If we interpret this literally, it means that the superconducting state is strongly gapless with large portions[14] of the Fermi surface, or even all of it, surviving in the superconducting state. The 'zero-field' superconducting transition in $ZrZn_2$ is fundamentally different to that in a conventional superconductor, because it occurs in the presence of ferromagnetism. The transition in $ZrZn_2$ has some similarities to the transition in a conventional superconductor for applied fields close to $\mu_0 H_{c2}$, where the superconducting anomaly is suppressed[15]. A second class of materials that show weak superconducting anomalies are the underdoped copper oxide[16] superconductors. A key characteristic of the superconducting transition in a ferromagnet may be the absence of a strong specific heat anomaly. Third, the superconductivity in $ZrZn_2$ is observed only within the ferromagnetic phase, which poses the question: what is the microscopic relationship between ferromagnetism and superconductivity[11,17,18]? We can exclude scenarios in which the superconductivity is due to inclusions of a second phase or a surface impurity, on the basis of thorough metallurgical tests and because the superconductivity and ferromagnetism disappear at the same pressure[19]. A macroscopic, that is, a uniform coexistence of the two states throughout the sample is consistent with the magnetic response we observe. In fact, an incomplete Meissner effect, that is, imperfect screening, is thought

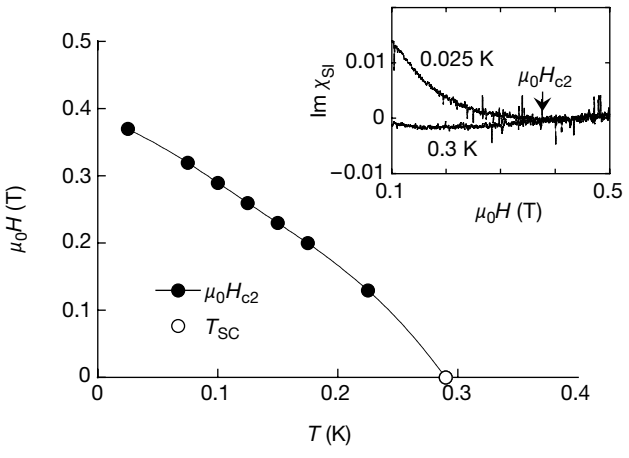

Figure 3 Superconducting phase diagram of $ZrZn_2$. Temperature dependence of the upper critical magnetic field $\mu_0 H_{c2}$ as derived from the dissipative part of the a.c. susceptibility, $Im\chi$. The value of $\mu_0 H_{c2}(T = 0)$ corresponds to a coherence length of $\xi = 290$ Å. We note that $\mu_0 H_{c2}$ is larger than the values of elemental Zr and Zn by two orders of magnitude, where T_{SC} of Zr and Zn are 0.875 K and 0.65 K, respectively. Inset, typical field dependence of the dissipative part of the a.c. susceptibility, $Im\chi$, used to determine $\mu_0 H_{c2}$.

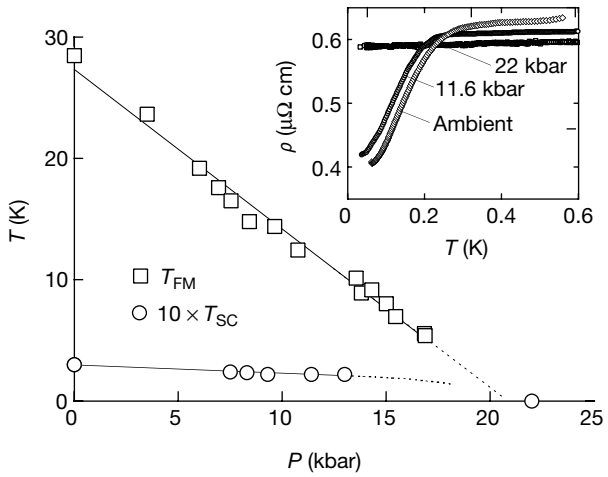

Figure 4 Pressure dependence of the ferromagnetic ordering temperature T_{FM} and superconducting ordering temperature T_{SC}. The pressure dependence of T_{FM} was determined in d.c. magnetization measurements. The pressure dependence of T_{SC} was determined from the resistivity, where typical curves are shown in the inset. Superconductivity disappears for $P > P_c = 21$ kbar, in the paramagnetic phase down to the lowest T measured, $T = 15$ mK. Note that T_{SC} for clarity is magnified by a factor of ten.

to be a signature of such a phase coexistence of superconductivity and ferromagnetism[20].

If metals close to a zero-temperature magnetic instability generally exhibit superconductivity, we might expect to observe this in a simple transition metal compound, as we have reported here. Our observations in $ZrZn_2$ contrast with materials such as $ErRh_4B_4$ (ref. 21) or the recently discovered $RuSr_2GdCu_2O_8$ (ref. 22) in which clearly distinguishable subsystems support either ferromagnetism or superconductivity. The presence of superconductivity throughout the entire pressure range for which ferromagnetism exists distinguishes $ZrZn_2$ clearly from UGe_2 (ref. 4), which is a strongly uniaxial 5*f* ferromagnet which shows a coexistence of superconductivity and ferromagnetism over a much smaller pressure range and is a member of a different class of materials. In contrast to these systems, the bands at the Fermi energy in $ZrZn_2$ are predominantly Zr 4*d* (ref. 6), and the magnetism and superconductivity derive from the same 4*d* electrons. Thus far we have said little about the details of the superconductive pairing mechanism. Both the longitudinal and transverse components of the susceptibility[5,7,8] are large for $ZrZn_2$ in the ferromagnetic state. This makes $ZrZn_2$ an excellent candidate for magnetically mediated pairing.

The most intriguing feature of the superconductivity in $ZrZn_2$ is that it only occurs in the presence of ferromagnetism and is hence promoted by the ferromagnetic state. This may arise naturally in scenarios where the Cooper pairs are in a parallel-spin (triplet) state, which is already favoured in the ferromagnetic state. Such behaviour could well be universal for itinerant ferromagnets in the limit of small Curie temperature and long electron mean free path. Our observations link several candidate classes of magnetically mediated superconductors in an unexpected way and suggest that fundamental notions concerning the relation of superconductivity and magnetic order need to be reexamined. □

Received 16 January; accepted 17 May 2001.

1. Ginzburg, V. L. Ferromagnetic superconductors. *Sov. Phys. JETP* **4,** 153–161 (1957).
2. Berk, N. F. & Schrieffer, J. R. Effect of ferromagnetic spin correlations on superconductivity. *Phys. Rev. Lett.* **17,** 433–436 (1966).
3. Mathur, N. D. *et al.* Magnetically mediated superconductivity in heavy fermion compounds. *Nature* **394,** 39–43 (1998).
4. Saxena, S. S. *et al.* Superconductivity on the border of itinerant–electron ferromagnetism in UGe_2. *Nature* **406,** 587–592 (2000).
5. Matthias, B. T. & Bozorth, R. M. Ferromagnetism of a zirconium–zinc compound. *Phys. Rev.* **109,** 604 (1958).
6. Jarlborg, T., Freeman, A. J. & Koelling, D. D. Self-consistent spin-polarized energy band structure and magnetism in $ZrZn_2$ and $TiBe_2$. *J. Magn. Magn. Mater.* **23,** 291–292 (1981).
7. Bernhoeft, N. R., Law, S. A., Lonzarich, G. G. & Paul, D. McK. Magnetic excitations in $ZrZn_2$ at low energies and long wavelengths. *Phys. Scr.* **38,** 191–193 (1988).
8. van Deursen, A. P. J. *et al.* A Fermi surface study of $ZrZn_2$. *J. Magn. Magn. Mater.* **54,** 1113–1114 (1986).
9. Enz, C. P. & Matthias, B. T. p-state pairing and the ferromagnetism of $ZrZn_2$. *Science* **201,** 828–829 (1978).
10. Fay, D. & Appel, J. Coexistence of p-state superconductivity and itinerant ferromagnetism. *Phys. Rev. B* **22,** 3173–3182 (1980).
11. Blagoev, K. B., Engelbrecht, J. R. & Bedell, K. S. Effect of ferromagnetic spin correlations on superconductivity in ferromagnetic metals. *Phys. Rev. Lett.* **82,** 133–136 (1998).
12. Smith, T. F., Mydosh, J. A. & Wohlfarth, E. P. Destruction of ferromagnetism in $ZrZn_2$ at high pressure. *Phys. Rev. Lett.* **27,** 1732–1735 (1971).
13. Mackenzie, A. P. *et al.* Extremely strong dependence of superconductivity on disorder in Sr_2RuO_4. *Phys. Rev. Lett.* **80,** 161–164 (1998).
14. Karchev, N. I., Blagoev, K. B., Bedell, K. S. & Littlewood, P. B. Coexistence of superconductivity and ferromagnetism in ferromagnetic metals. *Phys. Rev. Lett.* **86,** 846–849 (2001).
15. Sanchez, D., Junod, A., Muller, J., Berger, H. & Levy, F. Specific heat of 2H-$NbSe_2$ in high magnetic fields. *Physica B* **204,** 167–175 (1995).
16. Loram, J. W., Mirza, K. A., Cooper, J. R., Liang, W. Y. & Wade, J. M. Electronic specific heat of $Yba_2Cu_3O_{6+x}$ from 1.8 to 300 K. *J. Supercond.* **7,** 243–249 (1994).
17. Fulde, P. & Ferrell, R. A. Superconductivity in a strong exchange field. *Phys. Rev. A* **135,** 550–563 (1964).
18. Larkin, A. I. & Ovchinnikov, Y. N. Inhomogenous state of superconductors. *Sov. Phys. JETP* **20,** 762–769 (1975).
19. Huang, S. Z., Wu, M. K., Meng, R. L. & Chu, C. W. Hydrogen effect on the itinerant ferromagnets $TiBe_2x$ and $ZrZn_{1.9}$. *Solid State Commun.* **38,** 1151–1153 (1981).
20. Sonin, E. B. & Felner, I. Spontaneous vortex phase in a superconducting weak ferromagnet. *Phys. Rev. B* **57,** R14000–R14003 (1998).
21. Fischer, O. & Maple, M. B. (eds) *Superconductivity in Ternary Compounds* (Springer, Berlin, 1982).
22. Felner, I., Asaf, U., Levi, Y. & Millo, O. Coexistence of magnetism and superconductivity in $R_{1.4}Ce_{0.6}Ru_2Sr_2O_{10-\delta}$(R=Eu and Gd). *Phys. Rev. B* **55,** R3374–R3377 (1997).
23. Schreurs, L. W. M. *et al.* Growth and electrical properties of $ZrZn_2$ single crystals. *Mater. Res. Bull.* **24,** 1141–1145 (1989).

Acknowledgements

We thank A. Griffiths for resistivity measurements, P. Pfundstein and V. Ziebat for the microprobe analysis, H. Stalzer for SQUID magnetization measurements below 1 K, and A. D. Huxley, M. B. Maple and G. Müller-Vogt for discussions. Financial support by the Deutsche Forschungsgemeinschaft (DFG), the European Science Foundation (ESF) under the FERLIN programme, and the UK Engineering and Physical Sciences Research Council (UK-EPSRC) is gratefully acknowledged.

A possible nitrogen crisis for Archaean life due to reduced nitrogen fixation by lightning

Rafael Navarro-González*, Christopher P. McKay† & Delphine Nna Mvondo*

* *Laboratorio de Química de Plasmas y Estudios Planetarios, Instituto de Ciencias Nucleares, Universidad Nacional Autónoma de México, Circuito Exterior, Ciudad Universitaria, Apartado Postal 70-543, México Distrito Federal 04510, Mexico*

† *Space Science Division, NASA-Ames Research Center, Moffett Field, California 94035-1000, USA*

Nitrogen is an essential element for life and is often the limiting nutrient for terrestrial ecosystems[1,2]. As most nitrogen is locked in the kinetically stable form[3], N_2, in the Earth's atmosphere, processes that can fix N_2 into biologically available forms—such as nitrate and ammonia—control the supply of nitrogen for organisms. On the early Earth, nitrogen is thought to have been fixed abiotically, as nitric oxide formed during lightning discharge[4–6]. The advent of biological nitrogen fixation suggests that at some point the demand for fixed nitrogen exceeded the supply from abiotic sources, but the timing and causes of the onset of biological nitrogen fixation remain unclear[7–11]. Here we report an experimental simulation of nitrogen fixation by lightning over a range of Hadean (4.5–3.8 Gyr ago) and Archaean (3.8–2.5 Gyr ago) atmospheric compositions, from predominantly carbon dioxide to predominantly dinitrogen (but always without oxygen). We infer that, as atmospheric CO_2 decreased over the Archaean period, the production of nitric oxide from lightning discharge decreased by two orders of magnitude until about 2.2 Gyr. After this time, the rise in oxygen (or methane) concentrations probably initiated other abiotic sources of nitrogen. Although the temporary reduction in nitric oxide production may have lasted for only 100 Myr or less, this was potentially long enough to cause an ecological crisis that triggered the development of biological nitrogen fixation.

Because biological nitrogen fixation is energetically expensive and does not occur if adequate supplies of fixed nitrogen are available, it has been generally thought that the development of metabolic pathways to fix nitrogen arose only in response to a crisis in the supply of fixed nitrogen on the early Earth. This sudden reduction may have occurred soon after the origin of life[7–10] as the prebiotic source of organic material was depleted by the emerging life forms. In this scenario, the abiotic sources of fixed nitrogen were unable to sustain even simple microbial ecosystems. But many modern microbially dominated ecosystems are satisfied with abiotic inflows of fixed nitrogen and do not express nitrogen fixation; thus nitrogen fixation may have arisen much later[11], once biological demand had